Universidad
Carlos III de Madrid

FORCE GENERATION IN FLAPPING WINGS: A PARAMETRIC STUDY

Author: Maria del Mar Carrillo Galera
Tutor: Marco Raiola
Degree: Bachelor's Degree in Aerospace Engineering

ABSTRACT

This project consists in a parametric study of force generation in flapping wings.

The first part is a summary of the current state-of-the-art and socio-economic impact of this field of study, focusing on its main application: the micro-air vehicles. This is followed by a short explanation of the regulatory framework concerning this research.

After that, a brief explanation of the kinematics of plunging and pitching airfoils, the experimental set-up and the considered variables from the parametric space is done. For this study, three variables will be considered: the flapping frequency, the mean angle of attack and the pitch amplitude.

This is followed by an explanation of the force testing procedures, together with the experimental set-up found problems.

Finally, the reached results, physical meanings and conclusions are followed by an estimation of the necessary budget to develop this research.

CONTENTS

1. INTRODUCTION

1.1. Socio-economic environment

Flapping wings are easily found in nature, such as in birds, insects and some marine creatures (like fish and cetaceans).

Nowadays, there is an increasing interest in the aerodynamics of this wing configuration due to its possible application to a wide range of engineering problems, like the development of small air vehicles.

Several studies about the aerodynamics of small birds and insects have found that pitching and plunging wings provide an improved manoeuvrability and efficiency compared to the traditional fixed and rotatory wings at low Reynolds numbers [1], [2].

Micro air vehicles (MAVs) are flying vehicles with less than 15 cm wing span which are designed to operate at low speeds and thus, low Reynolds numbers [1]. The concept of MAVs has a significant interest due to its wide range of possible applications.

In the military field, they provide real-time combat information and target finding without risking soldiers' lives.
From a non-military point of view, their relevant potential uses are high risk indoor operations; such as pipeline inspections, search and rescue, road accident documentation and space exploration among others [2].

For this reason, a deep comprehension in the aerodynamics of flapping wing flight is crucial in order to improve the design of these devices.

1.2. Literature review

Although there is an increase in the research of flapping wing configurations, the interest on them has been present for centuries. Coming from Leonardo Da Vinci's flying machine in about 1505-1506, he tried to imitate the flight of birds with man powered ornithopters [3]. He realized that this system was too large and heavy to be efficient, but he set the foundation of this field of study.

It was not until the 1900s when a solid research to characterize the flapping wing aerodynamics was initialized. In 1909 and 1912, Knoller [4] and Betz [5] recognized that an aerodynamic force was generated in a plunging and pitching airfoil and that it could be decomposed into thrust, in the direction of flight, and lift, perpendicular to the direction of flight.

The first actual theoretical analyses of the aerodynamics of 2D flapping airfoils in forward flight were reported by Theodorsen [6], Garrik [7] and Von Kármán and Sears [8] .

The three studies assumed a flat-plate airfoil and potential flow theory, which means plane wake vorticity and negligible disturbances.

In 1935, Theodorsen [6] managed to find an analytical solution in a form that represents the transfer function between the angle of attack and the lift, only applicable to sinusoidal motions.

The given expression for the lift coefficient is:

$$cl(t) = \pi b\left(\frac{\dot{\alpha}}{U_\infty} + \frac{\ddot{h}}{{U_\infty}^2} - \frac{ba\ddot{\alpha}}{U_\infty^2}\right) + 2\pi C(k)\left[\frac{\dot{h}}{U_\infty} + \alpha + b\left(\frac{1}{2} - a\right)\frac{\dot{\alpha}}{U_\infty}\right] \qquad (1.1)$$

Where α is the angle of attack, b is the half of the wing chord, a is the pitch axis location relative to the mid-chord measured in semi-chords, $U_\infty$is the free-stream velocity and $C(k)$ is the Theodorsen function, which is complex-valued and dependent in the reduced frequency, $k$defined as:

$$k = \frac{\pi f c}{U_\infty} \qquad (1.2)$$

Where $f$is the motion frequency.

One year later, Garrik [7] used Theodorsen's approach and he determined that the drag produced in a flapping wing is the result of two contributions: the leading-edge suction and the pressure force acting along the airfoil.

$$cd(t) = -(\pi S^2 + \theta(t)cl(t)) \qquad (1.3)$$

Where θ is the pitch angle and S is the leading-edge suction.

The first term represents the leading-edge suction and the second one is the projection of the pressure force in the flight direction.

In 1938, Von Kármán and Sears [8] studied the lift generation of 2D airfoils. He used the classical airfoil thin theory assuming that a planar wake was formed.

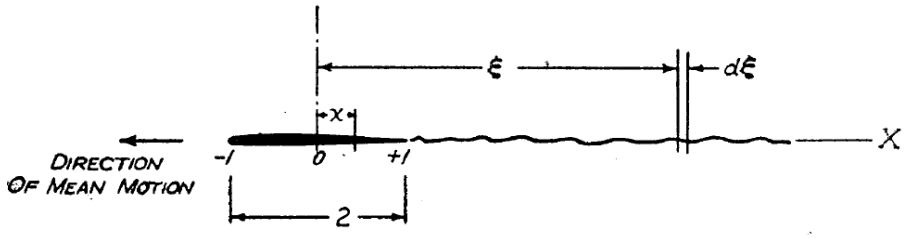

Figure 1. Used notation by Von Kármán and Sears [8]

The vorticity around the airfoil produced by a vortex located at ζ and with intensity Γ is given by:

$$\gamma(x) = \frac{1}{\pi}\frac{\Gamma}{\zeta - x}\sqrt{\frac{1-x}{1+x}}\sqrt{\frac{\zeta+1}{\zeta-1}} \qquad (1.4)$$

Integrating the wake vorticity, the lift mathematical expression was finally found:

$$L = -\rho\frac{d}{dt}\int_{-1}^{1}\gamma(x)xdx + \rho U\Gamma + \rho U\int_{1}^{\infty}\frac{\gamma(\zeta)d\zeta}{\sqrt{\zeta^2-1}} \qquad (1.5)$$

He stated that the lift had three contributions:

- The apparent-mass lift produced by the time rate of change of the vorticity
- The quasi-steady lift, which is the lift force that would be produced if the motion was stationary
- Lift produced by the wake vorticity

In the past years, several authors have also proposed methods to analyse the aerodynamic forces in terms of their contributions.

According to Chang [9], Martín-Alcántara [10] and more recently, Moriche et al. [11], the total aerodynamic force can be decomposed in three different contributions:

$$\vec{F} = \overrightarrow{F_m} + \overrightarrow{F_v} + \overrightarrow{F_s} \qquad (1.6)$$

Where $\overrightarrow{F_m}$ is the contribution due to the airfoil motion, $\overrightarrow{F_v}$ is the vorticity within the flow and $\overrightarrow{F_s}$ is the surface vorticity.

Moriche et al. [11] found that the main contribution corresponds to the flow vorticity followed by the body motion. The least important contribution is the surface vorticity, conclusion also reached by Martín-Alcántara [10].

An important flow characteristic found in flapping wings is the formation of vortices at the airfoil leading and trailing edges. Lewin and Haj-Harri [12] investigated how the interaction between the leading and trailing edge vortices influenced the propulsive efficiency. It was found out that at non-zero angle of attack, the airfoil may produce thrust apart from lift.

In addition, Ellington et al. [13] stated that the formation of a leading-edge vortex (LEV) was the main lift enhancing mechanism.

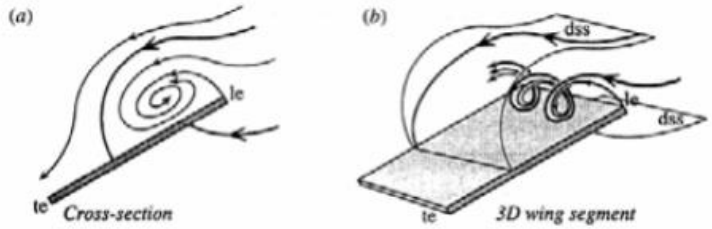

Figure 2. Leading edge vortex formation (adopted from [13]).

An increase in the lift force above its normal static value was produced as long as the LEV remained attached to the airfoil. This was followed by a sudden drop of the aerodynamic force when the LEV separated from the airfoil. This was proved in [13], where several airfoils of three different materials (Graphite, Monofilm and Latex) were tried and the lift coefficient was measured.

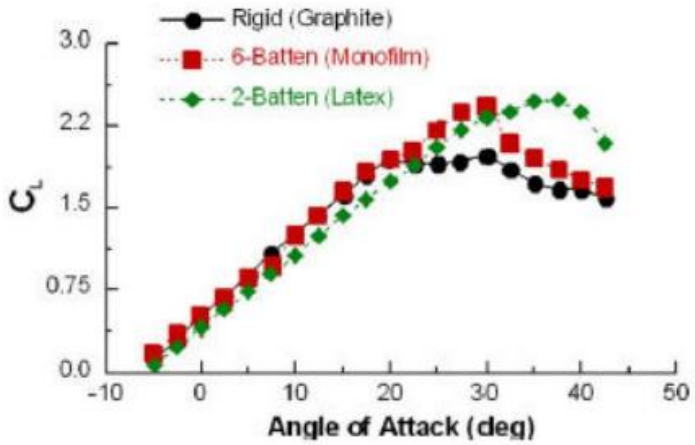

Figure 3. LEV lift enhancement (adopted from [13]).

As it can be seen, lift generation is improved in the Latex airfoil due to the LEV, whereas the LEV separates in the Graphite one, giving the same lift values as in the static condition.

The formation of a leading-edge vortex is also found in the research of McCroskey [14] in 1976 about the dynamic stall of helicopter blades, although at much higher Reynolds numbers than for MAVs applications. He defined dynamic stall as the flow separation and stall development that will occur in an oscillating airfoil that takes the effective angle of attack above its normal static value. Under these conditions, a vortical structure will be formed at the leading-edge generating a lift production enhancement and a delayed stall to higher angles of attack compared to the static conditions.

This dynamic stall vorticity was found to be quite similar to the leading-edge vortex formed in the investigation carried out by Ellington et al. [13], although dynamic stall is produced at considerably higher reduced frequencies and Reynolds numbers.

Carr et al. [15] also investigated the development of the dynamics stall process. The flow morphology is shown in figure 4.

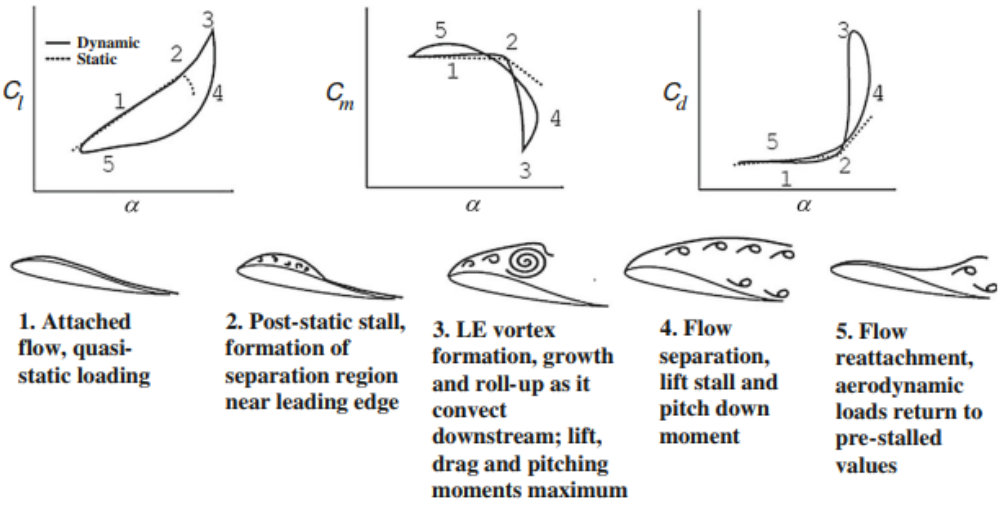

Figure 4. Flow morphology and unsteady airloads (adopted from [15]).

Lift stall occurs when the vortex passes into the wake, producing a dramatic drop in the generated lift, an increase of drag and a maximum nose-down pitching moment. Note that a hysteresis cycle is produced in the force and moment curves, mainly due to two contributions. The first one is a time lag in the flow reorganization from fully-separation until it is able to reattach again, which occurs at well below the static angle of attack. The second reason is another lag produced by the negative pitching moment, changing the pressure conditions at the leading-edge and causing a reverse kinematic effect called “induced camber”[16].

Focusing now on the leading-edge vortex separation, it has been explained with different models. For Dickinson and Gotz [17], the vortex separates when it reaches from 2 to 4 chord lengths of travel along the airfoil.

However, Gharib et al. [18] studied thrust generation with vortex rings created with a stream of fluid through a tube. It was stated that the vortex detachment occurred at the time called “formation number” whose value is 4. This was also corroborated by Krueger and Gharib [19] in 2003.

The formation number is a non-dimensional parameter that represents the instant when the vortex is not able to accommodate any more circulation.

It is defined as:

$$F = \frac{L}{D} = 4 \qquad (1.7)$$

Being D the tube diameter and L the distance travelled by the piston that creates the stream.

The vortex formed by the stream at the exit of the tube creates thrust until the formation number equals 4, time when the thrust reaches its optimum value. Then, the vortex ring stops forming, it detaches and the flow transforms into a quasi-steady jet followed by a vortex ring, reducing the thrust.

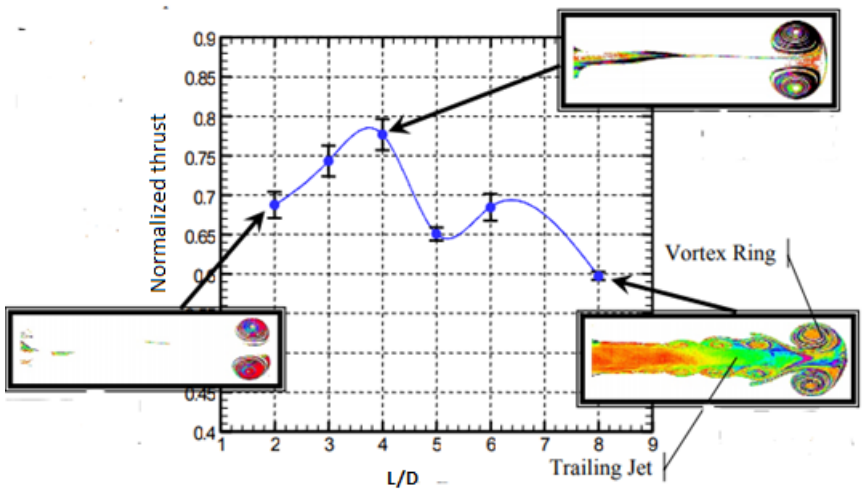

Figure 5. Average thrust optimization near the formation number. The plot is taken from [19] and the flow visualization from [18].

In addition, Daibiri [20] studied the applicability of this vortex ring to the flapping wing problem. He also identified an optimum vortex formation at a formation number of 4, point where the propulsion was maximized.

Last, but not least, there is another non-dimensional parameter that has a relevant effect in the flow dynamics: the Strouhal number, defined as:

$$St = \frac{2fh_o c}{U_\infty} \qquad (1.8)$$

where h_0 is the amplitude of the plunge motion.

In 1998, Anderson et al. [21] found that at St inside the range 0.25-0.35, a high propulsive efficiency was generated in the motion of pitching and plunging NACA 0012 airfoils.

Similar results were found some years later in the investigation of Read, Hover and Triantafyllou [22] in oscillating airfoils using different phase angles. The obtained thrust coefficients and propulsive efficiencies can be seen in figure 6, proving the previously said high efficiency Strouhal number range.

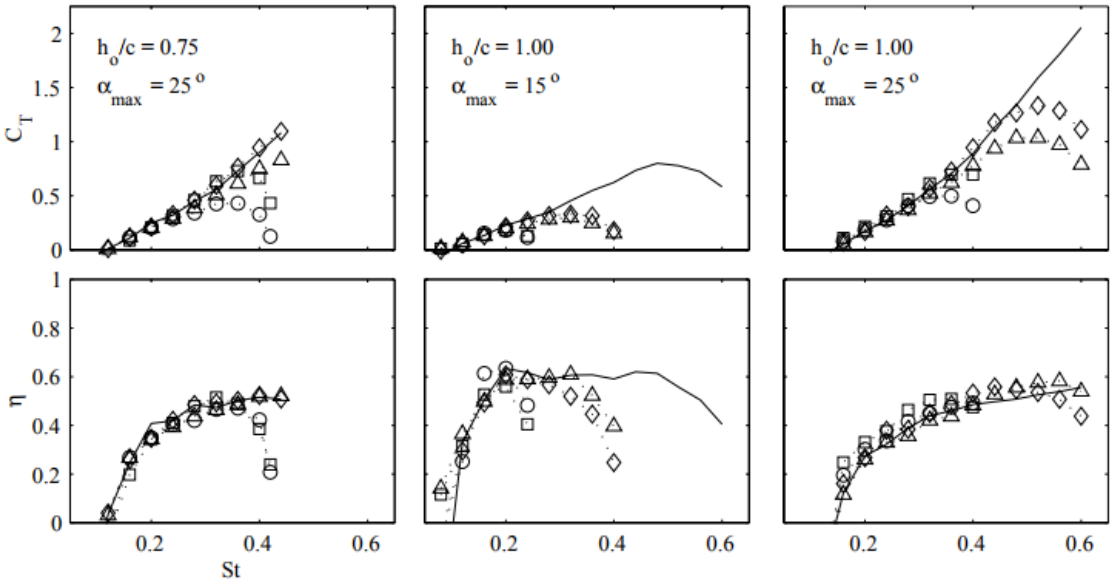

Figure 6. Thrust coefficient and propulsive efficiency obtained for phase angles 70º,90º and 100º (adopted from [22]).

The importance of the Strouhal number has also been investigated in flow visualization experiments using particle image velocimetry (PIV) and wake structure measurements, like Baik et al. [23] in 2012. It was found that the wake vorticity development was highly dependent on the value of the Strouhal number.

As it can be seen in figure 7, the LEV develops and detaches faster for smaller Strouhal numbers.

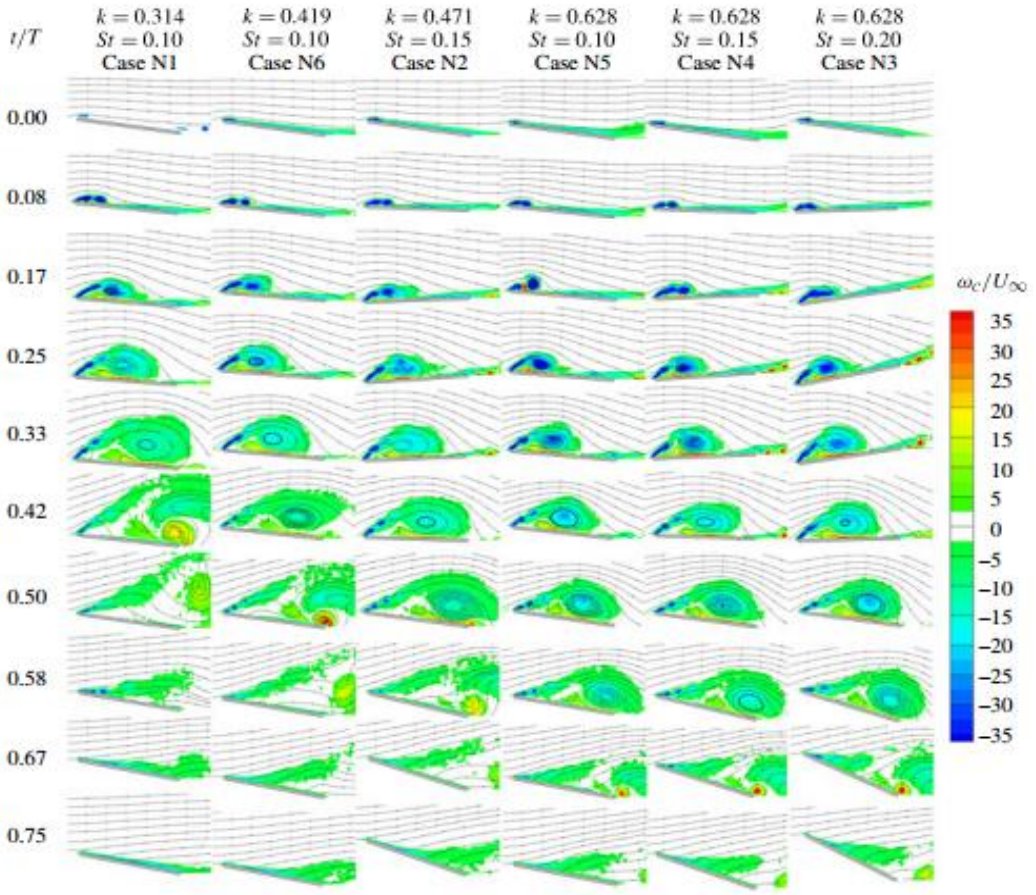

Figure 7. Effect of Strouhal number in the flow topology evolution (adopted from [23]).

1.3. Goals of the project

The aerodynamics of flapping wings have been widely studied, however there is a lack of parametric studies that try to gather conclusions on what the optimum configuration for force generation is.

For this reason, this research will be focused on the force generation of flapping wings at low Reynolds numbers. As this field has an extensive parametric space, this work will be just focused on the variation of three quantities: the Strouhal number, the pitch amplitude and the pitch mean angle.

In order to do so, an experimental research will be performed in the water tunnel facility located in the Aerospace Engineering Department of the University Carlos III de Madrid.

1.4. Regulatory framework

According to "Ley de Prevención de Riesgos Laborales (LPRL)" on its article number 16.2 [24], all companies (including universities) must write up a risk evaluation report including all the activities performed in their facilities. In addition, the "Reglamento de los Servicios de Prevención (RSP)" in its article number 4.2 [25], states that this report must be revised whenever the working conditions change.

As the water tunnel equipment was set up before the start of this project, the risk evaluation report was previously done and approved by the "Órgano de Evaluación de Proyectos (OEP)" according to the LPRL guidelines.

2. KINEMATICS AND KEY SCALING PARAMETERS

The flapping motion can be obtained as a combination of two different harmonic oscillations: pitching and plunging.

The pitching motion is the rotation about the wing pivot point. It is given by the following expression:

$$\theta(t) = \theta_m + \theta_0 \sin(2\pi f t + \phi) \qquad (2.1)$$

Where θ_m is the mean pitching angle, θ_0 is the pitching amplitude, f is the oscillation frequency and ϕ is the phase lag between the pitching and plunging motions, which for the present study has been set equal to 90°.

The plunge motion is the vertical wing displacement along the vertical axis and its mathematical expression is given by:

$$h(t) = h_0 \sin(2\pi f t) \qquad (2.2)$$

Where h_0 is the plunging amplitude.

The following illustrations (figures 8 and 9) describe the two displacements above stated:

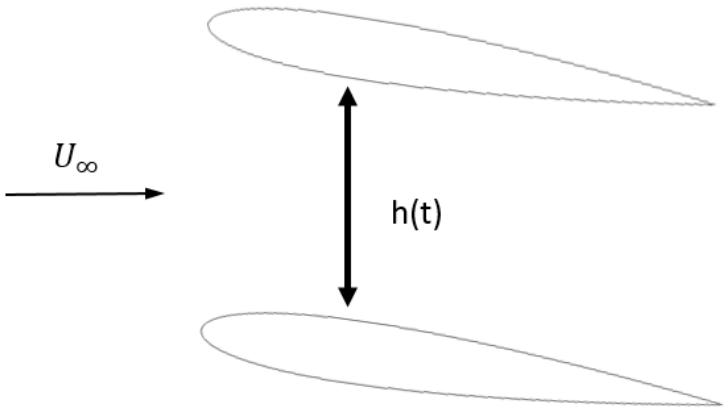

Figure 8. Plunge motion.

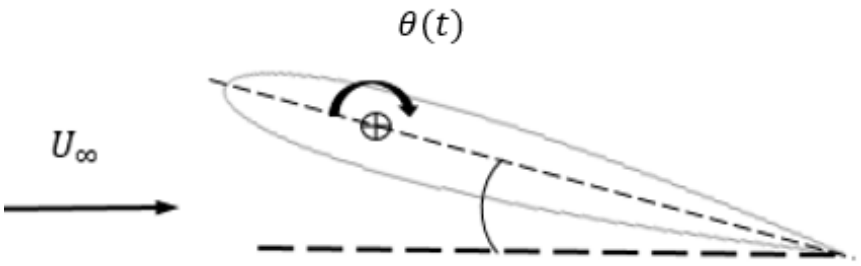

Figure 9. Pitch motion.

Considering both motions, the effective angle of attack seen by the airfoil is given by:

$$\alpha_{eff}(t) = \theta_m + \theta_0 \sin(2\pi f t + \phi) - atan\left(\frac{1}{U_\infty}\frac{dh}{dt}\right) \qquad (2.3)$$

In this way, this work is going to be focused on the 2D flapping motion problem with 2 degrees of freedom and a rigid airfoil.

As it can be seen, the wing motion is governed by the frequency (f), the free stream velocity (U_∞) , the airfoil chord (c), the plunge amplitude(h_0) and the air density (ρ) and kinematic viscosity (μ).

Making use of the Buckingham Pi theorem [26], three non-dimensional parameters can be found to simplify the problem and make it applicable to any problem regardless its dimensions.

Parameter	Symbol	Expression
Reynolds number	Re	$\frac{\rho U_\infty c}{\mu}$
Strouhal number	St	$\frac{2fh_o c}{U_\infty}$
Reduced frequency	K	$\frac{\pi f c}{U_\infty}$

Table 1. Non-dimensional parameters governing flapping motion.

3. SCOPE OF THE RESEARCH

The aim of the current study is to find an optimum configuration for force generation, or at least, a trend in its behaviour at low Reynolds numbers ($\sim 3500 - 3600$).

As the parametric space is quite big, the Reynolds number was fixed. Knowing the wing chord ($0.03\,m$) and assuming air as the working fluid (with dynamic viscosity of the order of $10^{-5}\,m^2/s$), the free-stream velocity was set to $0.12\,\frac{m}{s}$ for all the experiments.

In addition, although this velocity may seem low, if a higher value is selected, then the motion frequency needs to be increased in order to get a determined Strouhal number. This may create unwanted structural vibrations that can interfere in the force measurements.

Three flapping frequencies are considered in this study, $f = 0.2\,Hz$, $f = 0.4\,Hz$ and $f = 0.6\,Hz$. This together with this free stream velocity and knowing that the plunge amplitude is equal to the chord ($0.03\,m$), it gives three different Strouhal numbers: $St = 0.1, St = 0.2$ and $St = 0.3$. In the same way, the studied reduced frequencies are: $k = 0.157, k = 0.314$ and $k = 0.471$.

For each of the considered values of the Strouhal number, both the pitching amplitude and mean angle of attack were varied.

The pitching amplitude range is from 0° to 20° with a 5° increments division. The mean pitching angle range was decided to be from 0° to 15° with also a 5° increments division.

In this way, for each of the Strouhal numbers, 19 different cases were studied. Note that it should be 20, but the case with amplitude 20° and mean angle 15° was not studied to avoid the failure of the wing motion mechanism since it may not be able to support the high reached pitch angles.

The different studied cases are displayed in the following tables:

St = 0.1

		θ_0 (degrees)				
		0	**5**	**10**	**15**	**20**
θ_m (degrees)	**0**	Case 1	Case 2	Case 3	Case 4	Case 5
	5	Case 6	Case 7	Case 8	Case 9	Case 10
	10	Case 11	Case 12	Case 13	Case 14	Case 15
	15	Case 16	Case 17	Case 18	Case 19	

Table 2. Cases of study for St=0.1.

St = 0.2

		θ_0 (degrees)				
		0	**5**	**10**	**15**	**20**
θ_m (degrees)	**0**	Case 20	Case 21	Case 22	Case 23	Case 24
	5	Case 25	Case 26	Case 27	Case 28	Case 29
	10	Case 30	Case 31	Case 32	Case 33	Case 34
	15	Case 35	Case 36	Case 37	Case 38	

Table 3. Cases of study for St=0.2.

St = 0.3

		θ_0 (degrees)				
		0	**5**	**10**	**15**	**20**
θ_m (degrees)	**0**	Case 39	Case 40	Case 41	Case 42	Case 43
	5	Case 44	Case 45	Case 46	Case 47	Case 48
	10	Case 49	Case 50	Case 51	Case 52	Case 53
	15	Case 54	Case 55	Case 56	Case 57	

Table 4. Cases of study for St=0.3.

4. EXPERIMENTAL SET-UP

4.1. Water tunnel

At low speeds, typical for MAVs, compressibility effects do not affect the flow field. For this reason, the experiments could be carried out either in air or in water. However, water was finally selected as the working fluid because the measured force is an order of magnitude higher, so the resulting force resolution is also improved.

At a fixed Reynolds number, as the air and the water have different properties, the order of magnitude of the difference in the measured forces can be calculated:

$$\frac{F_w}{F_{air}} \approx \frac{\frac{1}{2}\rho_w U_w^2}{\frac{1}{2}\rho_{air} U_{air}^2} \approx 10 \qquad (4.1)$$

In this way, all the experiments were performed in the water tunnel facility property of the Department of Aerospace Engineering of the Universidad Carlos III de Madrid.

The water tunnel testing area cross section is 0.5 m high and 0.55 m wide with a free stream velocity up to $2\frac{m}{s}$.

4.2. Wing model

The wing model used was a flat-plate NACA0012 airfoil with a chord of 0.03 m. For these kind of airfoils, the ratio of thickness over chord is equal to $\frac{t}{c} = 0.12$, so the maximum thickness is 0.0036 m.

The wing is controlled horizontally from the top side of the water tunnel. Its span is 0.49 m, so it gives an aspect ratio of:

$$AR = \frac{b}{c} = \frac{0.49}{0.03} = 16.3 \qquad (4.2)$$

Where b is the wing span and c is the chord.

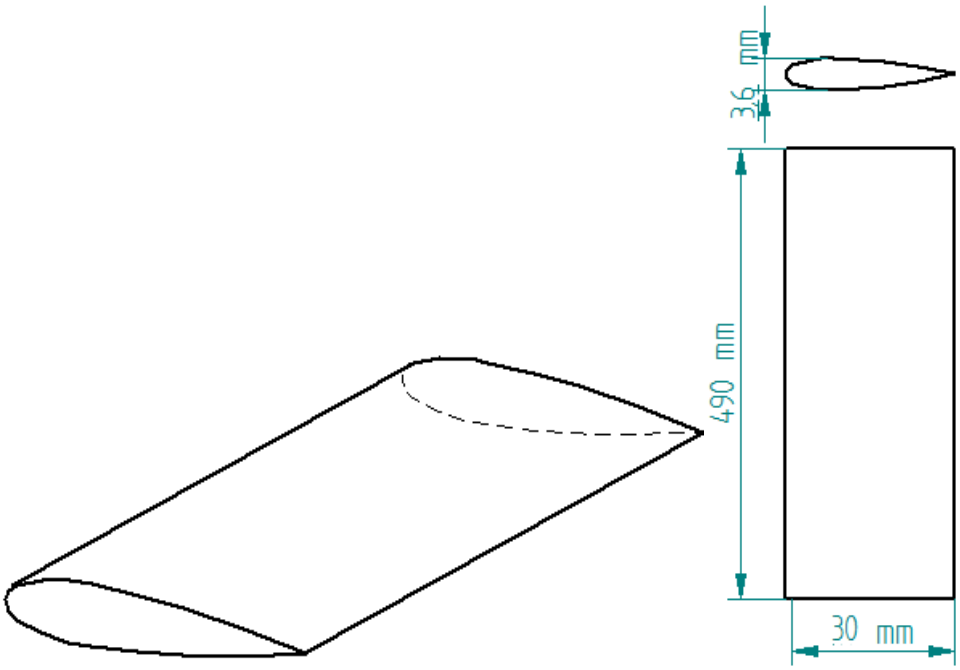

Figure 10 and Figure 11. 3D wing model and its dimensions.

As it can be seen, the aspect ratio is quite high; this, together with the fact that the wing tips are close to the tunnel walls, they reduce the 3D flow effects. Because of this, the flow can be considered as 2D in the middle part of the wing.

The wing material was Aluminium and its fabrication was carried out in a computer numerical control (CNC) machine with an accuracy of 0.01 *mm*.

4.3. Wing motion control

The system is composed of:

- A linkage formed by four rods.
- Two linear actuators
- Two motors
- Two controllers
- Two analog and digital I/O devices

The linkage is formed by four rods and it transmits the wing movement from the linear actuators motion. One rod is used to support the wing, two of them actually produce the pitching and plunging motions and the last one allows the pitching movement.

The linear actuators, model FESTO EGSK-26-100-6P, allow the motion of the four rods. Once the wing motion is started and fixed, the two linear actuators move in kinematic inversion to generate the pitching and plunging motion.

The electric motors, model FESTO EMME-AS-40-M-ASB, power the linear actuators.

The controllers (FESTO CMMP-AS-C2-3A-M0) provide the power to the motors and control their performance.

Finally, the I/O devices (DILIGENT Analog Discovery) send the signal between the user (through a computer run with a Python code) and the controllers by transforming the signal from digital to analog and the other way around.

In a nutshell, when the computer sends a task to be performed, it is transduced in the I/O devices and sent to the controllers.
Both I/O devices are also interconnected: the output of the first one serves as clock and it is connected to the trigger of the second one. In this way, the signal and the movements are synchronized.
The controller provides power to the motor and controls the motion of the actuators through it. In addition, it verifies that there are no errors in its performance.
The linear actuator is connected to the motor by a mechanical linkage and the actuator finally transmit the motion to the articulated rod mechanism.

4.4. Force measurement system

This system includes:

- An F/T sensor
- An InterFace/Power supply box (IFPS box)
- National Instruments Data Acquisition Card (NI-DAQ)

The sensor is a ATI Nano17 IP68 six degrees-of-freedom sensor. It is located between the wing and the rod mechanism. It has a maximum allowable force of 480 N in the z-axis and 250N in the x and y axis. The maximum torque is 1.8 Nm in the z-axis and 1.6 Nm in the x and y. The maximum frequency that the sensor can support is 2200 Hz [27].

As it can be expected for low Reynolds and Strouhal numbers, these values are out of the scope of the performed experiments.

According to the official web page of ATI Nano17 [27], the sensor has a sensitivity of $\frac{1}{320}N$ and $\frac{1}{64}\ Nmm$ for the force and the torque, respectively.

It must be also considered that the sensor with IP68 waterproofing is sensitive to the immersion depth, so a tare experiment with a low oscillation frequency will be carried out. This procedure will be explained in detail later.

The sensor is connected to the IFPS box, which sends 6 analog signals to the data acquisition card (DAQ NI USB-6210). They correspond to three force and three torque measurements (one for each of the axis).

The DAQ trigger is also connected to the output of the I/O device that serves as clock. In this way, the force measurements and the wing motion are synchronized. Finally, the DAQ sends the signals to a computer, where they are calibrated and traduced to the corresponding units.

4.5. Assembly to the wing and final set up

In order to attach the sensor to the wing and to the rod mechanism, a L-type support composed of two parts is used. This part and the load cell gave a distance between the wing and the first moving rod of 12 mm.

In this way, the centre of pitching is not on the wing; it is 12 mm vertically displaced. This will cause a horizontal velocity component of the wing during the pitching motion. For a rotation, it is known that the azimuthal velocity is given by:

$$V_h = r\dot{\theta} = r2\pi f\theta_0 \cos(2\pi f t + \phi) \qquad (4.5)$$

Where $r = 12\ mm$.

This velocity induces an unavoidable error in the measurements, however, the maximum value of this velocity will be 0.016 m/s for the performed experiments so it will not considerably affect the results.

The wing is held inside the tunnel with a structure that supports the actuators and places the wing in the middle of the testing section through a slot in the top wall of the tunnel.

The final assembly of all components is shown in the following figures. The first one is taken from a previous Uc3m student's thesis that helped to develop a similar flapping wing testing facility.

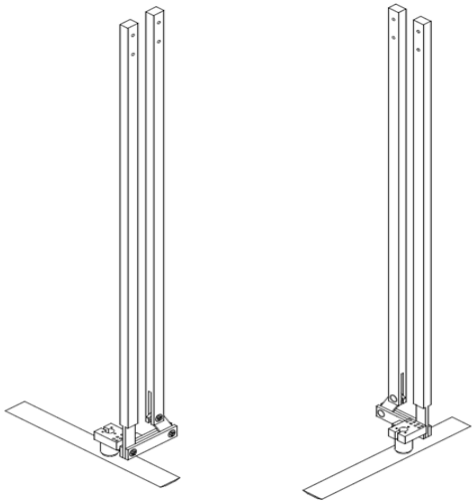

Figure 12. Sensor-wing-rods assembly. Taken from a past Uc3m student thesis [28].

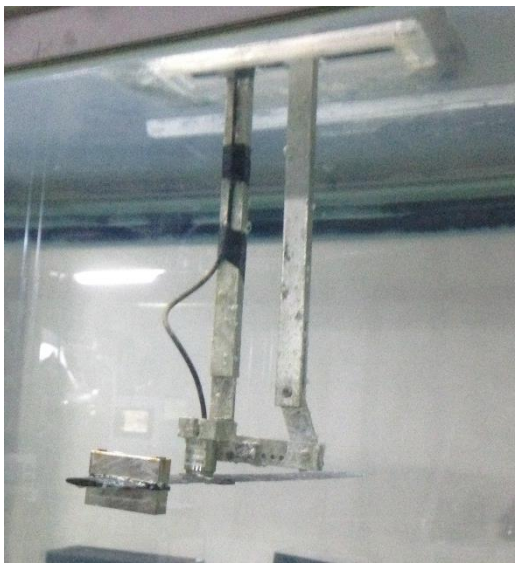

Figure 13. Sensor-wing-rods assembly placement in the testing section.

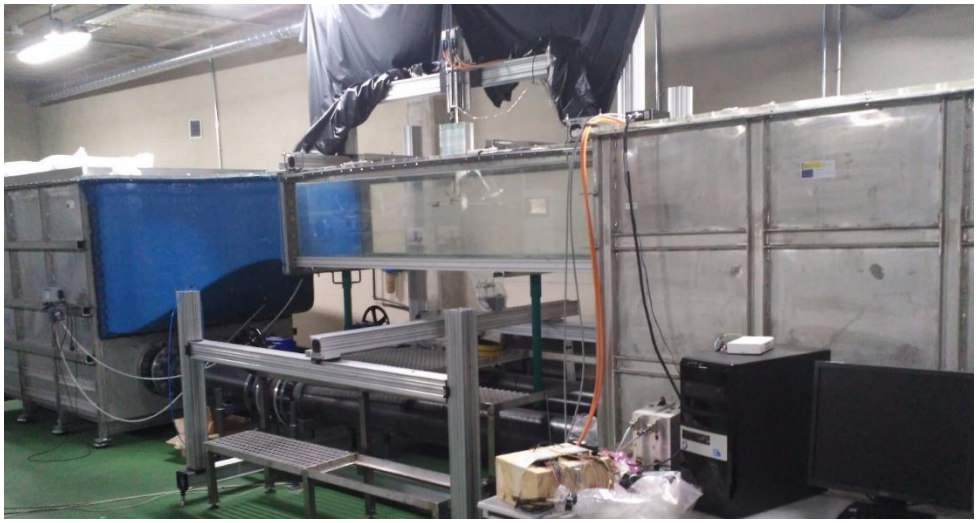

Figure 14. Final assembly.

5. FORCE PROCESSING AND FILTERING

As it was previously stated, the force recording and the wing motion are synchronized, which means that the force recording does not start until the wing passes through its initial position.

Each force sample consists in a text file with six columns corresponding to the forces and torques in each of the axis x, y and z. The data acquisition frequency was set to be 1000 Hz for all the cases. It must be also pointed out that the first 4 cycles were discarded in each measurement as doing this, it removes the transient initial error and it does not affect the final force results.

5.1. Inertia force removal

In order to compute the lift and drag forces, it is necessary to compute the hydrostatic force acting on the wing. However, when the experiments are performed in water at normal free-stream velocity, the sensor not only measures the hydrodynamic force, but also the inertia force due to the movement, the weight and buoyancy forces. Because of that, each force experiment consisted in four measurements:

- Tunnel full of water and at normal free stream velocity and frequency: This gave the hydrodynamic force together with the inertia, weight and buoyancy force acting on the wing.
- Tunnel full of water, zero free stream velocity and 1/10 of the oscillation frequency: This measurement was used to tare the sensor and remove its bias due to the IP68 waterproofing. As it was said before, the waterproofing makes the sensor reading sensitive to the water depth. In this way, the buoyancy force was removed.
- Tunnel with air at normal free stream velocity and frequency: It gives the inertial loads due to the wing motion.
- Tunnel with air, zero free stream velocity and 1/10 of the oscillation frequency: This last measurement serves to tare the inertial loads reading removing the weight force.

In this way, the tare measurements and the inertia force were subtracted from the force readings and aerodynamic forces respectively to give the hydrodynamic loadings.

$$F_{inertia} = F_{air_{dynamic}} - F_{air_{static}} \quad (5.1)$$

$$F_{hydrodynamic} = F_{water_{dynamic}} - F_{inertia} - F_{water_{static}} \quad (5.2)$$

5.2. Sensor and wing reference frames

To compute the lift and drag, it is necessary to know the relation between the sensor coordinate system and the free-stream coordinate system.
The sensor x-axis is aligned with the wing chord and z-axis with the plane normal to the wing as it can be seen in the following figure.

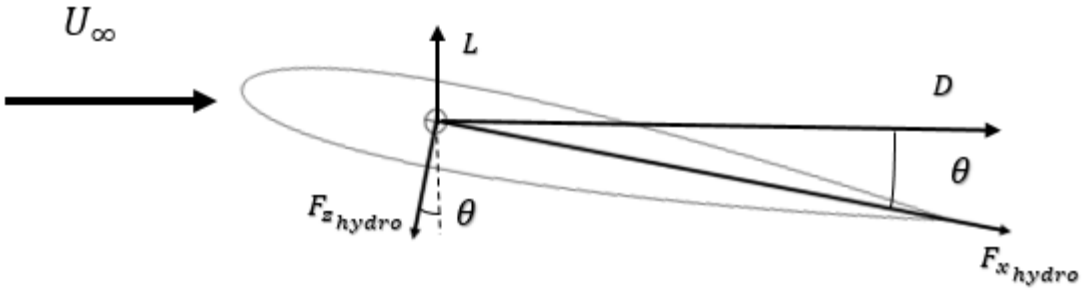

Figure 15. Coordinate system transformation.

As it can be seen, the hydrodynamic force was transformed from the sensor coordinate system to the free-stream coordinates using the pitching angle time story to get the lift and drag forces.

$$D = F_{x_{hydro}} \cos\big(\theta(t)\big) - F_{z_{hydros}} \sin(\theta(t)) \quad (5.3)$$

$$L = -F_{z_{hydro}} \cos\big(\theta(t)\big) - F_{x_{hydro}} \sin(\theta(t)) \quad (5.4)$$

Finally, the force coefficients were computed by normalizing the lift and drag with the dynamic pressure and the wing chord and span.

$$Cl = \frac{L}{\frac{1}{2}\rho U_\infty^2 S} \qquad Cd = \frac{D}{\frac{1}{2}\rho U_\infty^2 S} \quad (5.5) \text{ and } (5.6)$$

5.3. Found set-up problems and solution

First of all, a first long force recording was done for all cases with approximately 300 cycles in order to reduce the random error (as it decreases with the square root of the number of samples). However, an increasing bias in time was reported in the experiments performed in water.

As the sensor was turned on, the strain gauges inside it started emitting power proportional to the product of the square of the current and the gauge resistance. Note that this resistance changed in time as the loads acting on the wing changed.

This is the so called Joule's effect:

$$P \quad \alpha \quad I^2 \cdot R(t) \qquad (5.7)$$

The sensor bias under static conditions can be observed in figure 16.

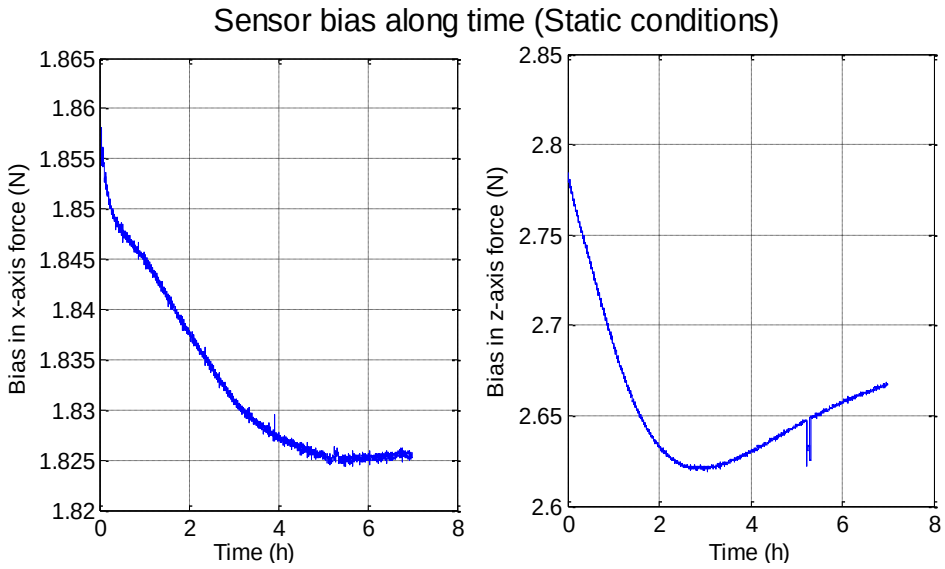

Figure 16. Sensor bias due to Joule's effect.

As the volume of water contained in the tunnel was too big, (approximately 550 liters), the bias does not reach a steady state plateau inside a reasonably time to perform the experiments.

This bias could be also observed in the previously obtained force data measurements subtracting the last value of each force reading to the next force data file acquired.

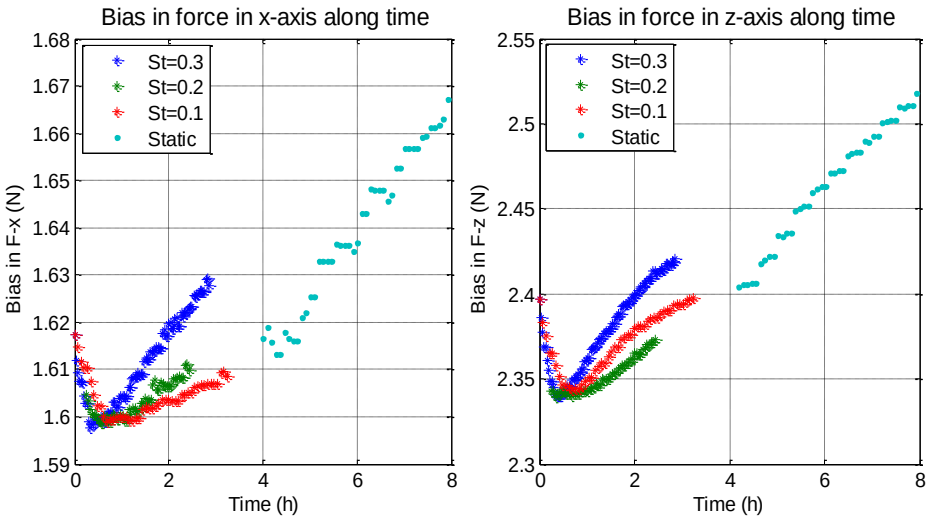

Figure 17. Fund bias in the force data measurements.

Note that the slope of the curve is greater for the case with the highest Strouhal number (St=0.3) as the faster wing motion speeds up the heat transfer. Also, the effect is considerably more noticeable in the z-axis than in the x-axis.

Because of this effect, the right procedure that should be used is:

- The long force recording that was kept and detrended (reducing its mean to zero) in order to calculate the force fluctuation phase in a cycle.

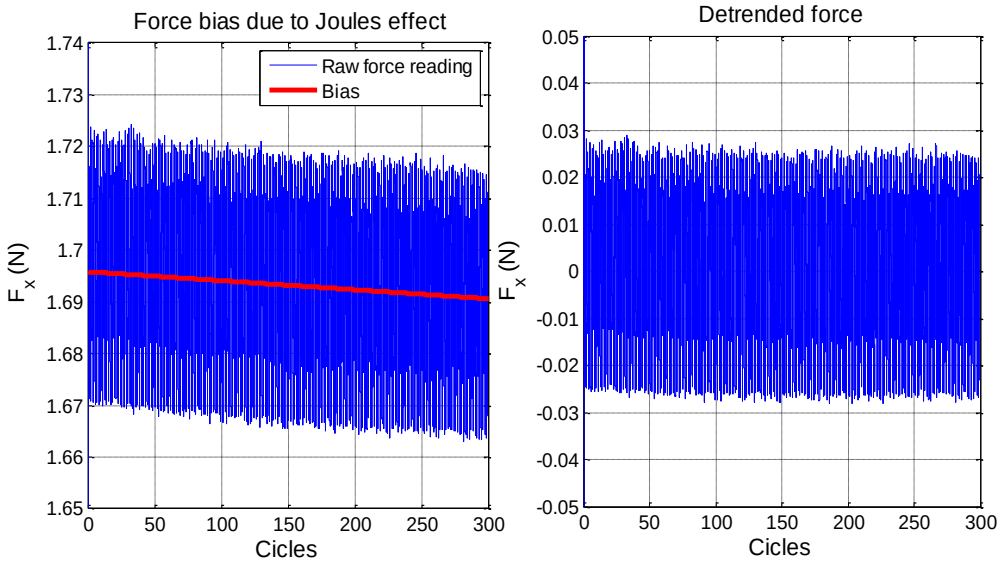

Figure 18. Force reading bias and detrending effect.

- Another shorter experiment was performed to compute the force time average. The dynamic measurement in water was followed by the static one, such that the time between them is minimum. In this way, the bias is smaller and the error can be easily quantified.

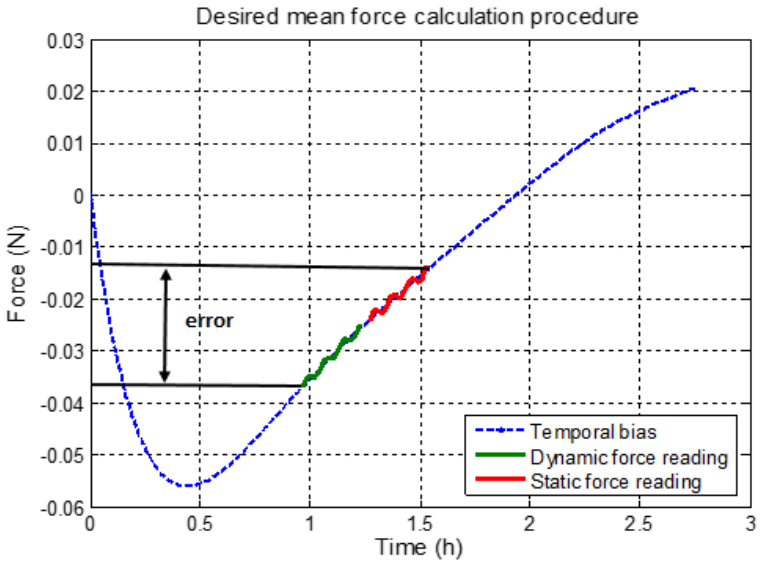

Figure 19. Desired mean force calculation procedure.

- Finally, the force fluctuation and the time average were summed up to compute the final force generated in a cycle.

Unfortunately, it was not possible to repeat the measurement with this testing procedure since the sensor stopped working properly.

Another possible solution was thought in order try to fix in some way the problem:

- The long force recording was kept and detrended to compute the force fluctuation as in the previous testing procedure.

- As no more experiments could be done, the same force recordings were utilized to compute the force average values. Using the bias curves previously shown in figure 17, together with the time at which the force data files were created, an estimation of the bias affecting a particular force recording could be done and removed by interpolating the bias curves. From that, the mean force generated was computed.

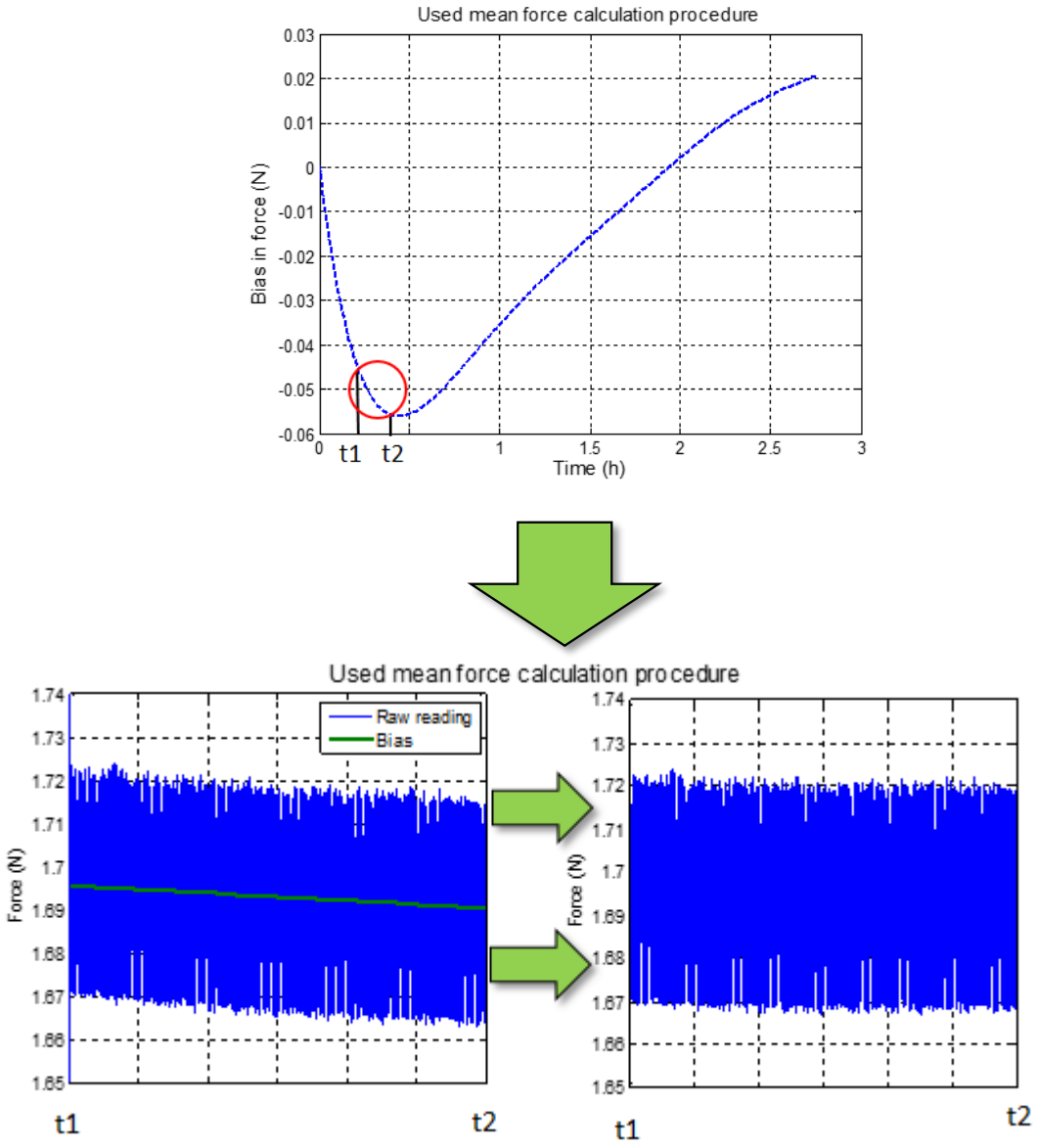

Figure 20. Used mean force calculation procedure.

As several days were used to perform the force measurements, a bias curve was generated for each of them. In this way, the experimental error due to the external ambient conditions was in some way reduced. These curves were also used to estimate the maximum possible error; this will be deeper explained in section 5.5.

5.4. Signal filtering

Some filtering had to be used as the raw force recording had a lot of noise.

5.4.1. Butterworth filter

All recorded samples were filtered with a second-order low-pass Butterworth filter to remove the signal noise coming from the structural resonance of the wing and the external sources. The cutoff frequency was set equal to five times the corresponding flapping frequency since the signal was properly filtered. In this way, the used cutoff frequencies are $f_c = 1\ Hz, f_c = 2\ Hz$ and $f_c = 3\ Hz$, corresponding to the three considered flapping frequencies, $f = 0.2\ Hz,\ f = 0.4\ Hz$ and $f = 0.6\ Hz$.

In addition, the cutoff frequencies were normalized with half of the value of the data sampling frequency (1000 Hz).

$$w_c = \frac{5 f_{flapping}}{\frac{f_{sampling}}{2}} \qquad (5.8)$$

The filter Bode plot is shown in figure 21; as it can be observed, the filter attenuates any signal with a frequency higher than a given cutoff frequency.

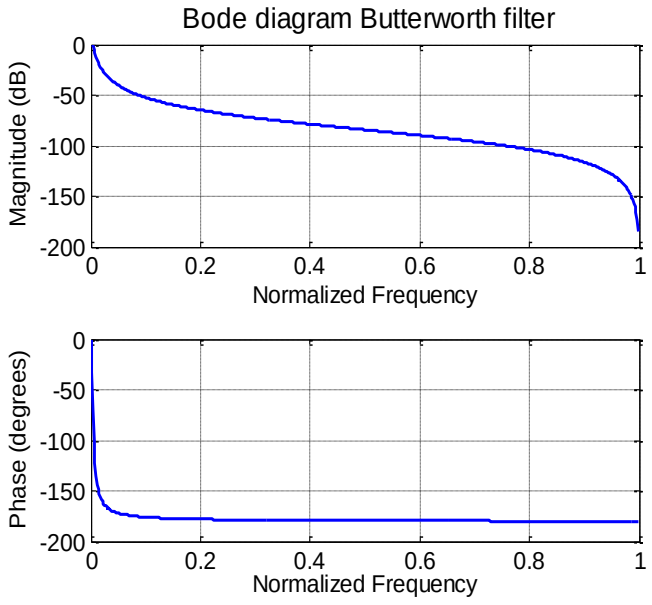

Figure 21. Butterworth filter Bode plot.

The effect that the Butterworth filter has in the force signal is as follows in figure 22.

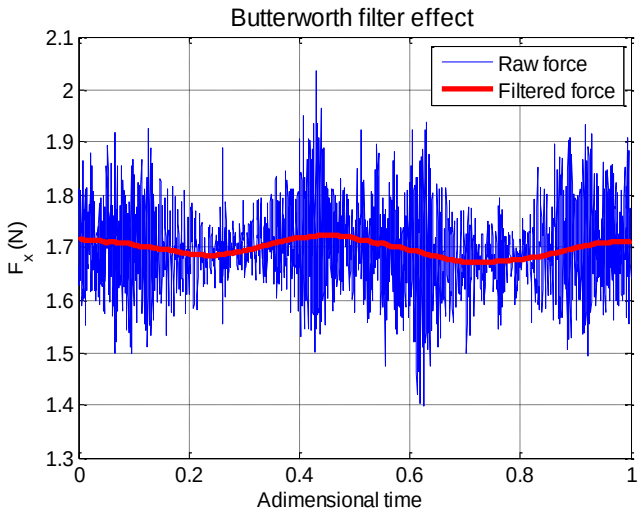

Figure 22. Butterworth filter effect in the force reading.

As it can be observed, most of the noise is removed from the raw force reading.

5.4.2. Mean in cycles

After detrending the raw force signal or removing the Joule's effect bias, more noise is removed by performing the mean between the approximately 300 cycles recorded. The effect can be seen in figure 23.

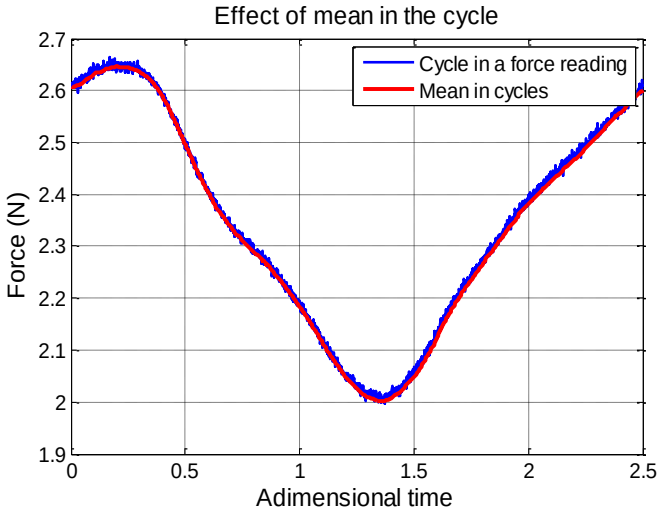

Figure 23. Mean in cycles effect in the force reading.

5.5. Error estimation

Two types of errors will appear in the force measurements: the bias error and the random error or sensitivity.

Starting with the bias error, if the time at which the experiment started and finished is known and the corresponding bias curve is used, the error can be estimated by subtracting the points where it crosses the bias curve.

Also, the maximum possible error that a measurement can have is the difference between the maximum and minimum of the bias curve.

This is illustrated in figure 24.

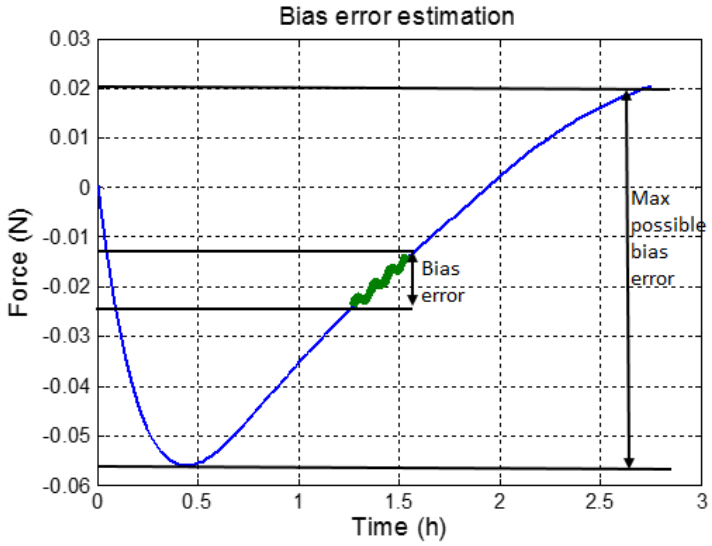

Figure 24. Bias error estimation.

It must be noticed that the maximum errors will be found in the case of higher motion frequency, as the slope of the curve was steeper as shown in figure 17.

The bias errors were tried to be removed from the force measurements, however, as the used procedure explained in section 5.3 is not the most adequate, some error might still be present.

The second error will be coming from the sensor sensitivity. As this is a random error, it can be easily removed with just performing a long measurement, as it decreases with the square root of the number of samples. In section 4.4, it was mentioned that the force and torque sensor sensitivities were $\frac{1}{320}\ N$ and $\frac{1}{64}\ Nmm$, respectively.

Normalizing them with the dynamic pressure and the wing area and chord, the force and torque coefficient sensitivity can be computed.

$$S_{C_f} = \frac{S_f}{\frac{1}{2}\rho S U_\infty^2} = \frac{\frac{1}{320}}{\frac{1}{2}\cdot 1000 \cdot 0.0147 \cdot 0.12^2} \cong 0.03 \qquad (5.9)$$

$$S_{C_m} = \frac{S_m}{\frac{1}{2}\rho S U_\infty^2 c} = \frac{\frac{1}{64}\cdot 10^{-3}}{\frac{1}{2}\cdot 1000\cdot 0.0147\cdot 0.12^2\cdot 0.03} \cong 0.005 \qquad (5.10)$$

Note that this will be the sensitivity error found if a single cycle force reading was made. However, as 300 cycles were taken and it decreases with the square root of the number of samples, it can be neglected from the force coefficients.

6. RESULTS

In this section, the effects that the parameters have in the force coefficient fluctuation part and its physical meaning will be studied. To see their influence, a set of cases of interest will be selected varying only the parameter to be studied and leaving the rest fixed. The other cases will be shown in an annex attached to this document.

For a better understanding of the flow physics, both the force coefficients as a function of the adimensional time (defined as the ratio of the time over the period) and the effective angle of attack will be studied.
In addition, the force coefficients standard deviation and their mean value will be calculated using the procedure explained in section 5.3.

But before all of this, the airfoil static force characterization will be shown in order to have a reference point to compare the force coefficient results.

6.1. Static characterization

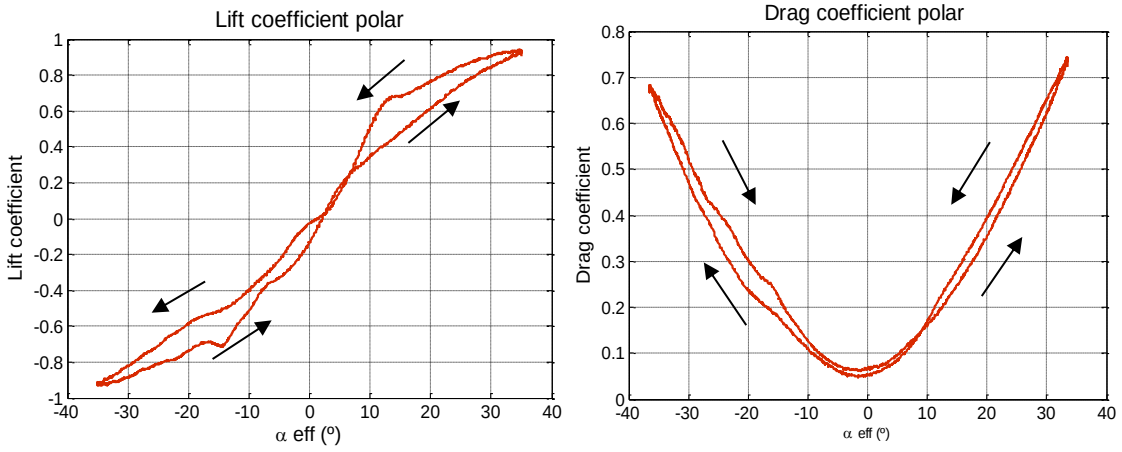

Figure 25. Airfoil static characterization.

Before performing all the force experiments, the static lift and drag curves were obtained by giving the airfoil a pitching motion (without plunge) at a very slow frequency.

The arrows show the direction of the movement. Note that the lift curves during the downstroke and the upstroke are not the same as when the flow detaches, it does not immediately stick again to the airfoil, producing this hysteresis effect.

The lift curve can be considered as symmetric about half motion period, but the drag curve is slightly asymmetric due to the flow being affected by the sensor. Note that both of them should be symmetric as it was observed in the study of Sunada et al. [29] about airfoil characteristics at low Reynolds numbers. The hysteresis is very small and the lift coefficient has a linear behaviour, whereas the drag coefficient is more quadratic.

6.2. Lift and drag coefficients fluctuating part as a function of time

6.2.1. Effect of the pitching amplitude

In order to analyse the effect of θ_0, two different Strouhal numbers with the same mean pitching angle will be chosen. Also, the effective angle of attack and the pitching angle time stories will be plotted to offer a better explanation of the behaviour of the lift and drag coefficients.

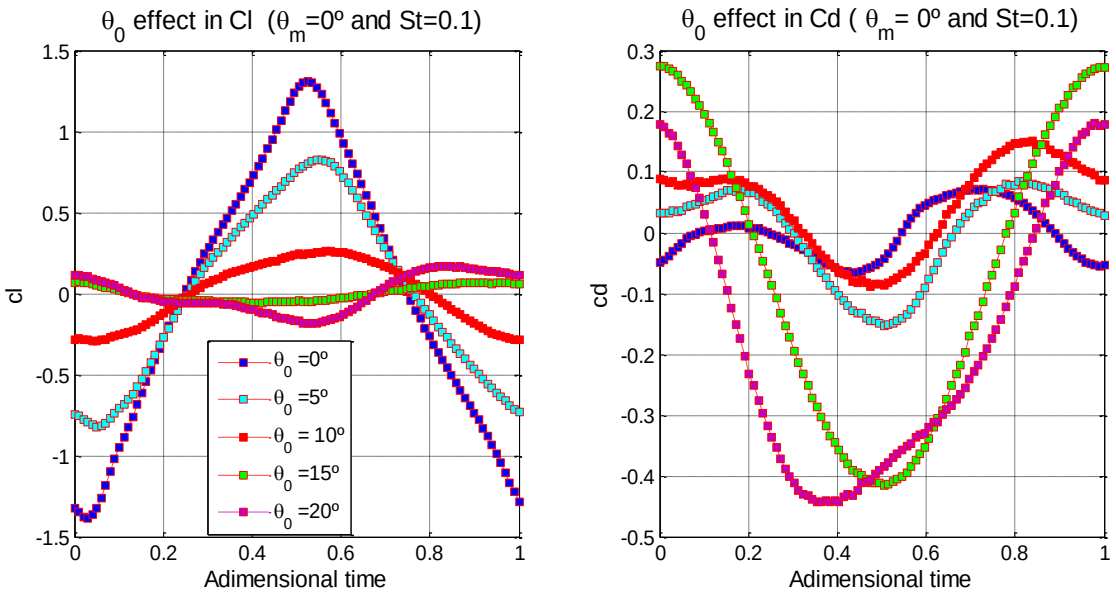

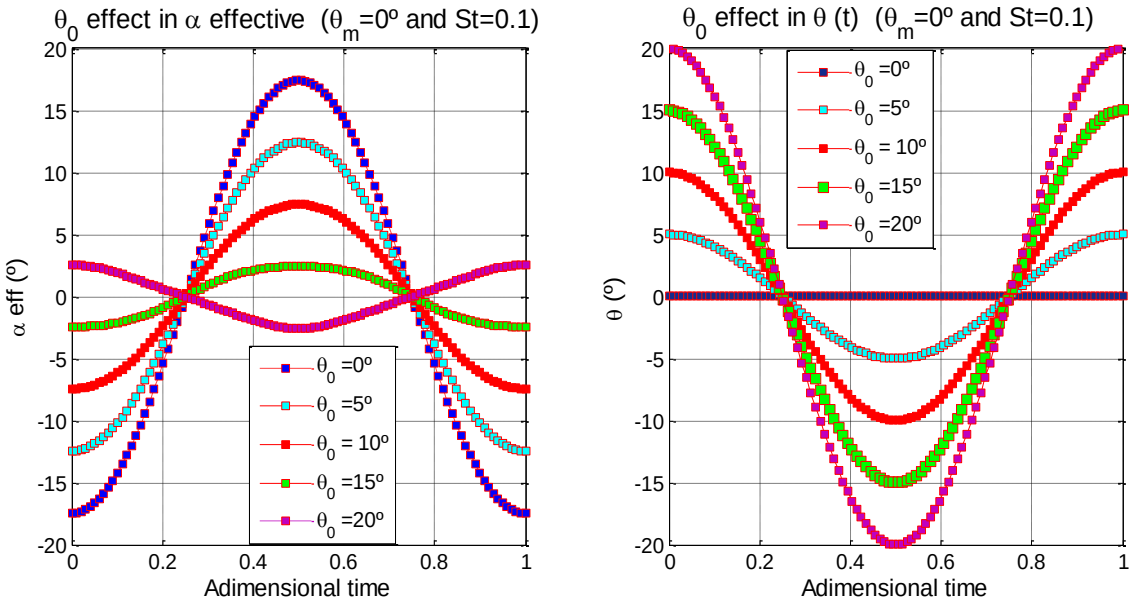

Figure 26. Pitch amplitude effect in lift and drag coefficients, effective angle of attack and pitch angle with St=0.1 and $\theta_m = 0°$.

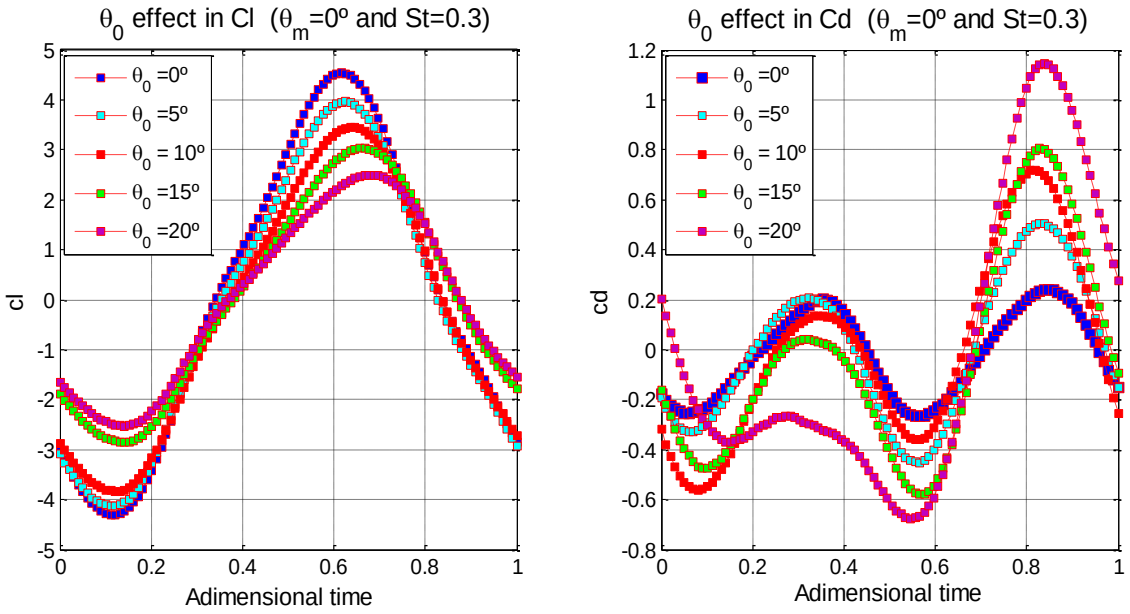

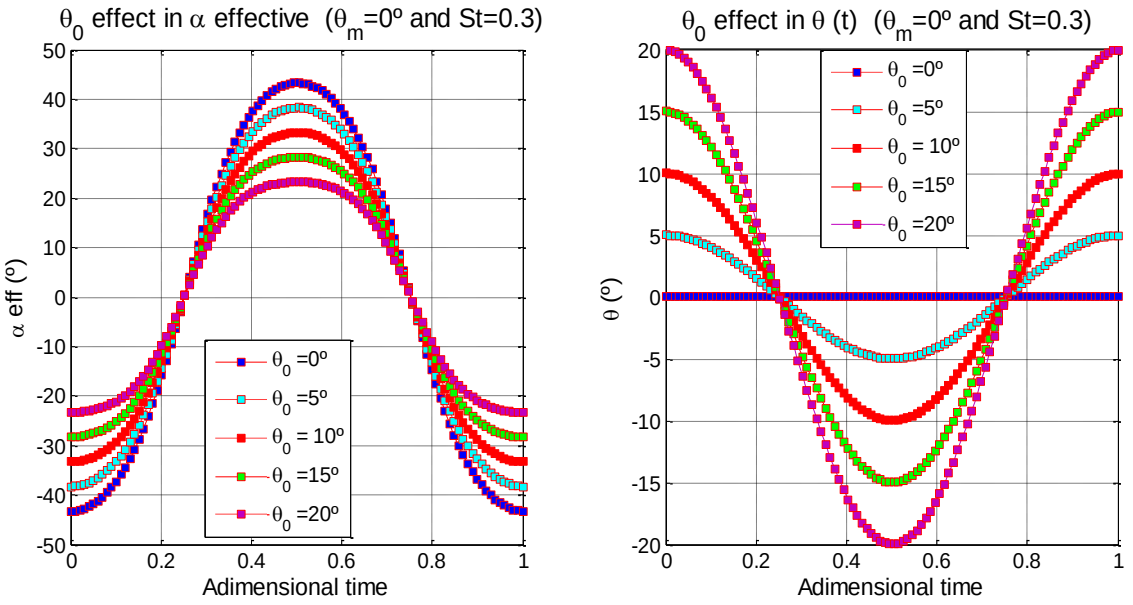

Figure 27. Pitch amplitude effect in lift and drag coefficients, effective angle of attack and pitch angle with St=0.3 and $\boldsymbol{\theta_m = 0°}$.

As it can be seen, the effective angle of attack reduces its amplitude as the pitch amplitude, θ_0 increases, totally the opposite behaviour is observed in the pitch angle, $\theta(t)$. In addition, with a lower Strouhal number, the effective angle of attack maximum amplitude decreases generating an inverted peak for St= 0.1 and $\theta_0 \geq 15°$.

The fact that the lift and drag coefficients fluctuation have this shape is related to the projection of the resulting aerodynamic force.

Several authors, such as Chang [9], Martín-Alcántara et al. [10] and Moriche et al. [11], have tried to explain this aerodynamic force as the contribution of three different sources: the body motion (or added-mass term in the unsteady potential flow), the vorticity within the flow and the surface vorticity (or viscous effects).

In the research of Moriche et al. [11], it was found that the main contribution to the aerodynamic force was due to the vorticity within the flow, followed by the added-mass force contribution. The viscous effects did not play a relevant role.

Taking this into account, it can be assumed that the aerodynamic force is mainly perpendicular to the airfoil [11], then the lift and drag forces can be expressed as:

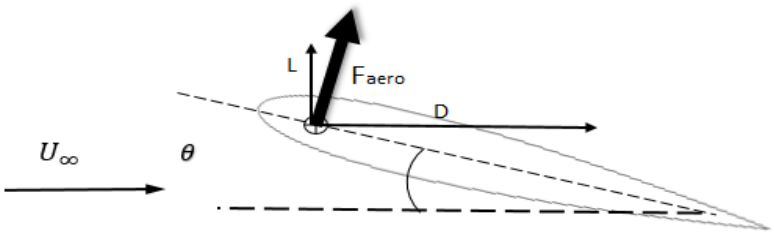

Figure 28. Aerodynamic force decomposition

$$L = cos\theta \cdot F_{aero} \quad where \quad cos\theta \approx 1 \tag{6.1}$$

$$D = \sin\theta \cdot F_{aero} \quad where \quad \sin\theta \approx \theta \tag{6.2}$$

Due to the force projection shown in figure 28, the lift is basically dominated by the effective angle of attack, whereas the drag is affected by both contributions: the effective angle of attack and the pitch angle.

Therefore, the lift coefficient curve gets flatter as θ_0 increases, being this effect greater for lower Strouhal numbers. This basically means that the effective velocity that the airfoil experiences is more aligned with the free-stream velocity and thus, lift is not generated as much as for lower values of θ_0.

Conversely, the drag curve increases its amplitude as θ_0 grows, mostly due to the contribution of the increase in the pitch angle.

6.2.2. Effect of the mean pitching angle

A similar procedure is now followed to study the effect of the mean pitch angle, θ_m.

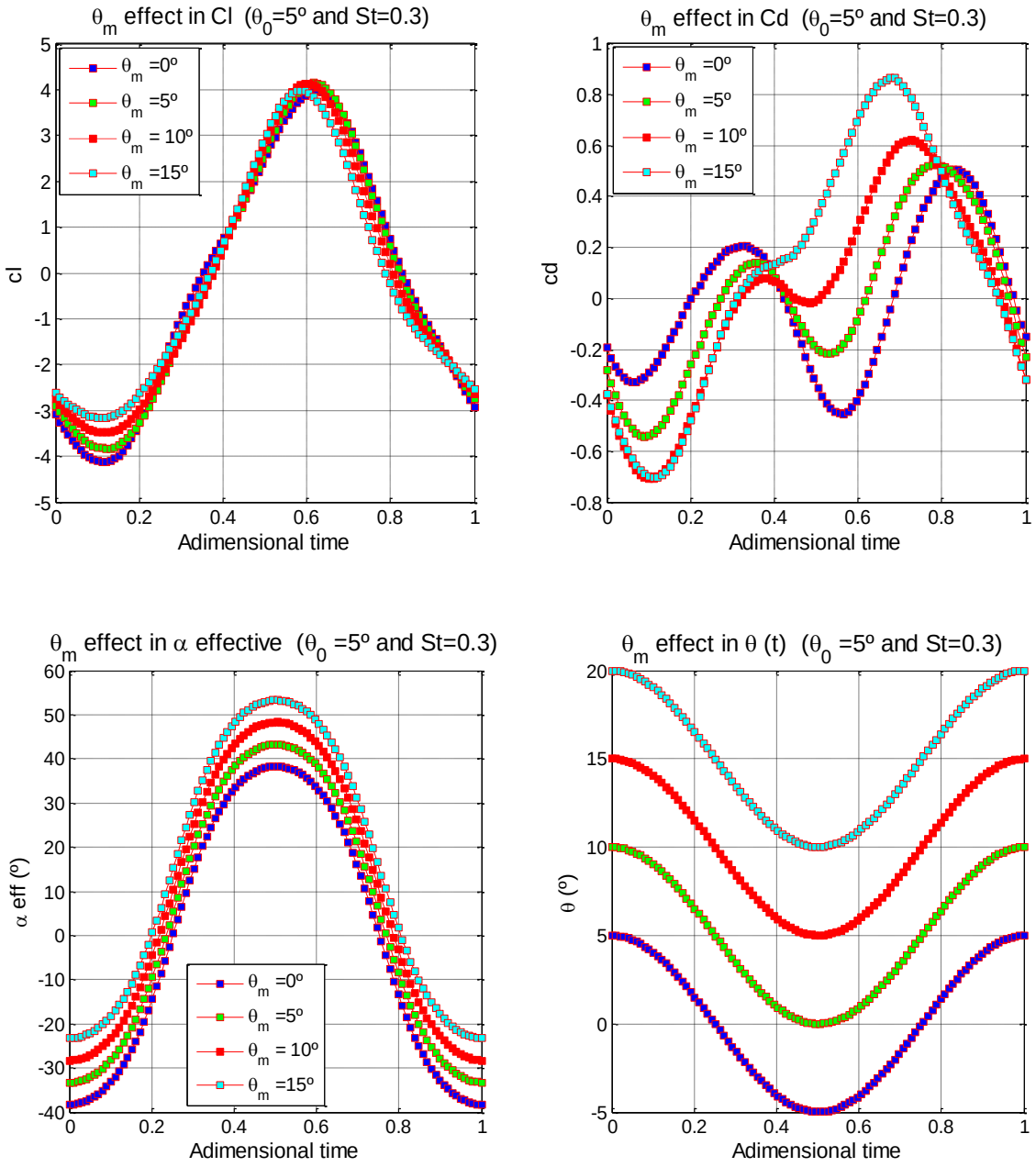

Figure 29. Mean pitch angle effect in lift and drag coefficients, effective angle of attack and pitch angle with St=0.3 and $\theta_0 = 5°$.

In this case, the effective angle of attack and the pitch angle are only shifted upwards with the increase in θ_m, being the effect in the effective angle o attack, α_{eff}, much weaker.

Following the same reasoning as before, as the lift is mainly dominated by α_{eff}, the lift coefficient curves will not be importantly affected by the change in θ_m.

Nevertheless, the increase in θ_m will make the amplitude of the drag coefficient curve to grow and loss its periodicity.

6.2.3. Effect of the Strouhal number

Finally, the effect of the Strouhal number is studied with the case of zero pitch mean and amplitude angle.

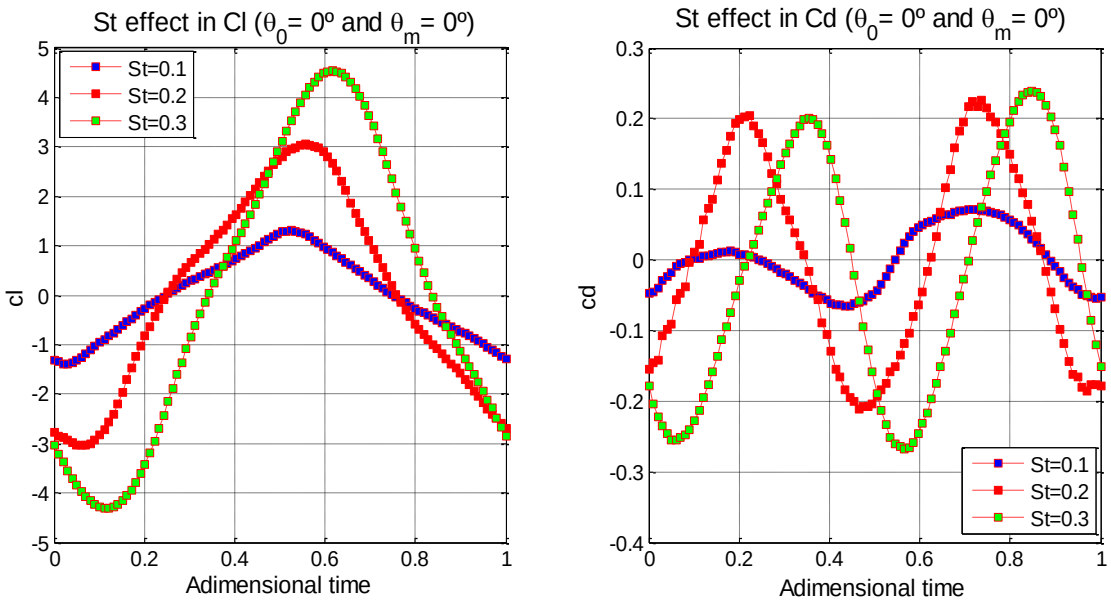

Figure 30. Strouhal number effect in lift and drag coefficients with $\theta_m = 0°$ and $\theta_0 = 0°$.

The effect of the Strouhal number is to create a phase shift and an overshoot in the lift and drag coefficient curves.

A similar overshooting behaviour was discovered by McCroskey et al. [14] due to the so called dynamic stall found in helicopters (although at higher Reynolds numbers).

According to McCroskey et al. [14], dynamic stall occurs when an airfoil has an unsteady motion (pitching or plunging) that takes the effective angle of attack above the normal static value.

Under these conditions, a vortex disturbance is formed at the leading-edge that enhances lift production provided it remains attached to the airfoil surface giving the same lift and drag overshoots that can be observed in this case.

The airfoil stall occurs at higher angles of attack than the normal static stall, producing a dramatic drop in the lift coefficient for further increase in the angle of attack.

In addition, Baik et al. [23] observed in their PIV investigation that the LEV formed at later times for higher values of the Strouhal number, giving also greater force overshoots. This behaviour is also observed in figure 30.

To make the effect of each parameter clearer, the following table sums up the information above explained.

	Increasing θ_0	Increasing θ_m	Increasing St
Cl	• Flattens graph	NO RELEVANT EFFECT	• Higher peak amplitude • Delayed peak formation
Cd	• Greater oscillation amplitude • Loss of periodicity	• Loss of periodicity	• Delayed peak formation • Higher amplitude

Table 5. Parameters variation effect in the lift and drag coefficients.

6.3. Lift and drag coefficient fluctuating part as a function of the effective angle of attack

In this section, the lift and drag coefficients curves fluctuating parts as a function of the effective angle of attack will be studied, identifying the effects that the change of the previous stated parameters have on them.

6.3.1. Effect of the pitching amplitude

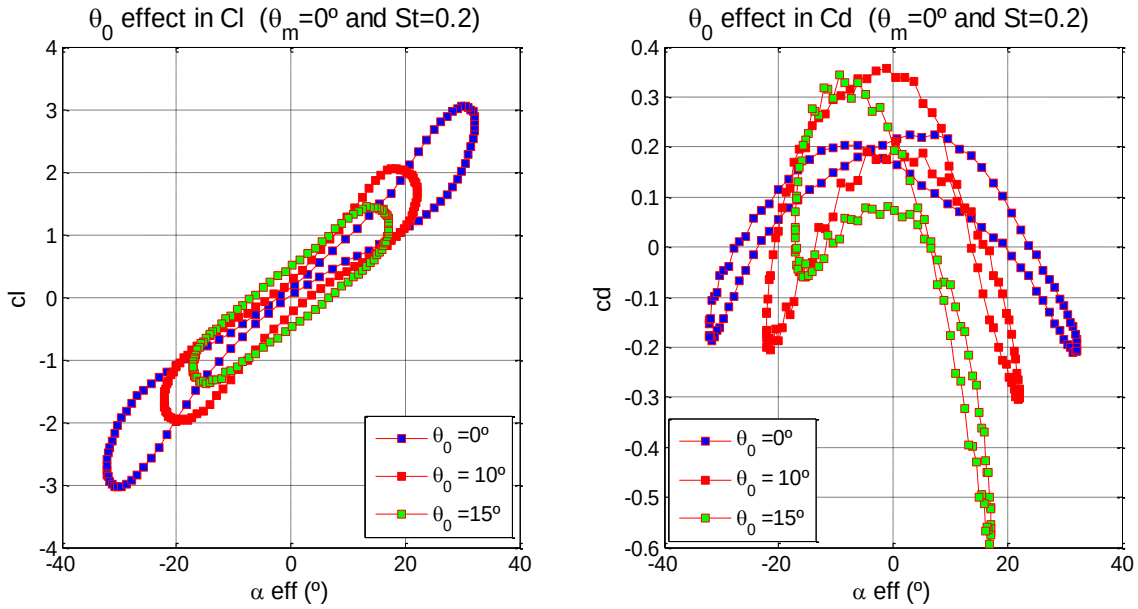

Figure 31. Pitch amplitude effect in lift and drag coefficients with St=0.2 and $\theta_m = 0°$.

As it can be seen, the increase in the pitch amplitude has three effects:

The first one is that it decreases the amplitude of the hysteresis cycle in the lift coefficient and increases the one of the drag coefficient.

Secondly, as θ_0 increases, the angle at which the stall occurs decreases. It must be noticed that the maximum lift or drag coefficients are not produced at the point where the effective angle of attack reaches a maximum, it occurs before. This is because as the stall occurs, the force coefficients abruptly decrease for higher angles of attack, as it was previously mentioned.

The third effect is that the drag coefficient curve loses its symmetry due to the influence of the pitch angle as it was explained in section 6.2.1. In addition, a negative peak is formed for the highest pitching amplitude, which may signify that thrust is being produced.

Another important point that must be mentioned is that the obtained force coefficients values are well above the static characteristic curves shown in figure 25, which is basically due to the lift enhancement due to the leading-edge vortex formation.

6.3.2. Effect of the mean pitching angle

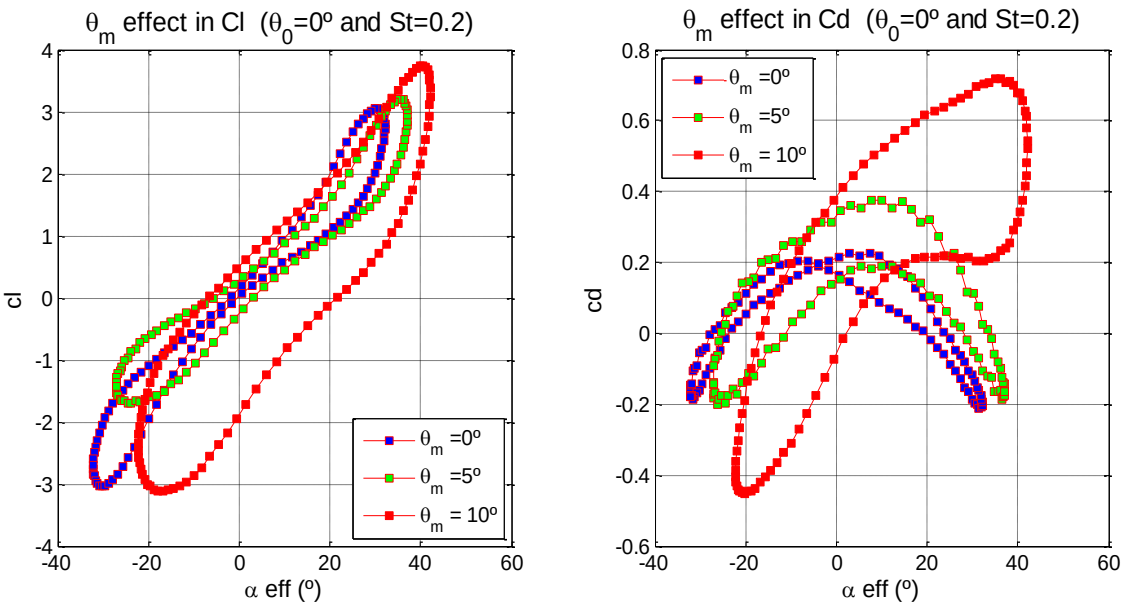

Figure 32. Mean pitch angle effect in lift and drag coefficients with St=0.2 and $\theta_m = 0°$.

Note that the maximum positive reached effective angle of attack has a greater absolute value than the negative minimum. As the mean pitch angle increases, the flow separates at a higher positive angle of attack but also at a smaller negative angle leaving in this way the curves centred at the corresponding θ_m.

Another interesting fact is that the hysteresis effects are more noticeable as the mean pitch angle increases. McCroskey et al. [14] and Carr et al. [15] found a relative similar behaviour by holding the oscillation amplitude and frequency and increasing the mean angle of attack. They identified two flow regimes: "light" dynamic stall, at the lowest mean angle, and "deep" dynamic stall, at the highest angle.

McCroskey [14] noticed a larger hysteresis effect at the "strong" dynamic stall, giving a physical explanation based on the fact that a higher mean angle of attack produced a greater part of the cycle inside the fully separated flow. Thus, a larger hysteresis was generated. He also stated that for a "strong" stall, fairly low angles of attack were needed for reattachment to occur. This behaviour is also observed in figure 32.

6.3.3. Effect of the Strouhal number

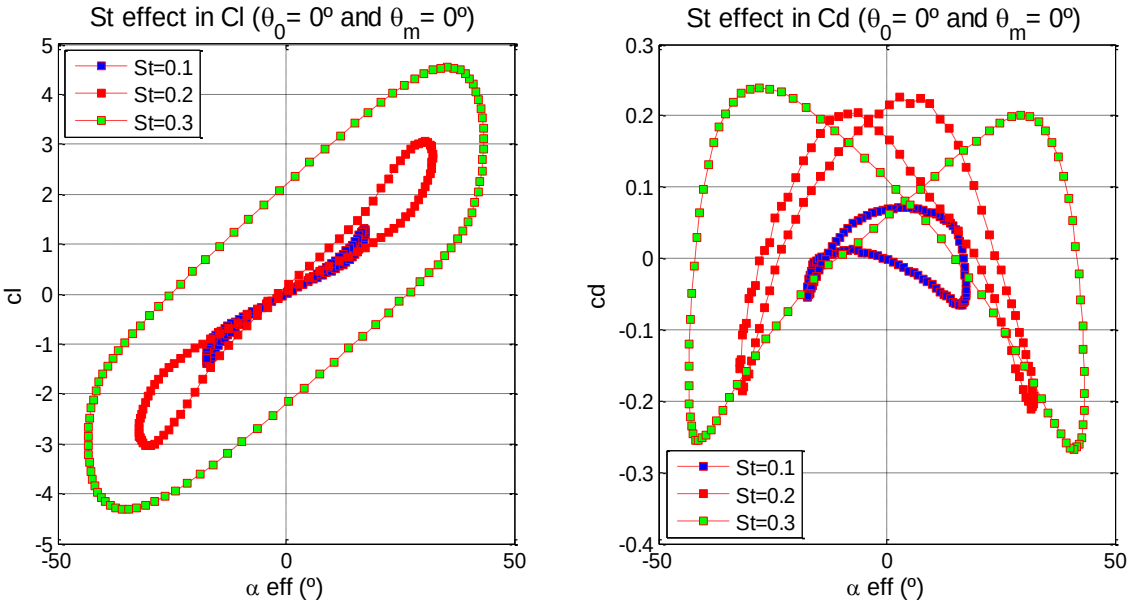

Figure 33. Strouhal number effect in lift and drag coefficients with $\theta_m = 0°$ and $\theta_0 = 0°$.

As the Strouhal number grows, the stall is delayed to higher effective angles of attack and producing also greater lift and drag coefficient values. This was also observed and physically explained in section 6.2.3. with the investigation carried out by Baik et al. [23].

The hysteresis cycle is also greater as the Strouhal number increases. In the book "Principles of Helicopters Aerodynamics" [30], a greater hysteresis is found if the reduced frequency is increased in the dynamic stall of helicopter blades. In addition, it states that as the hysteresis effect grows, a lower angle of attack is needed for the flow to reattach again.

6.4. Standard deviation

The standard deviation measures the dispersion of a set of data, or what it is the same, how close the data is to its mean value. A low standard deviation means that the data points are close to the average value of the whole sample.

Having a low standard deviation in the lift and drag coefficients can be important to avoid fatigue problems in the UAV structures and to improve the controllability of the devices.

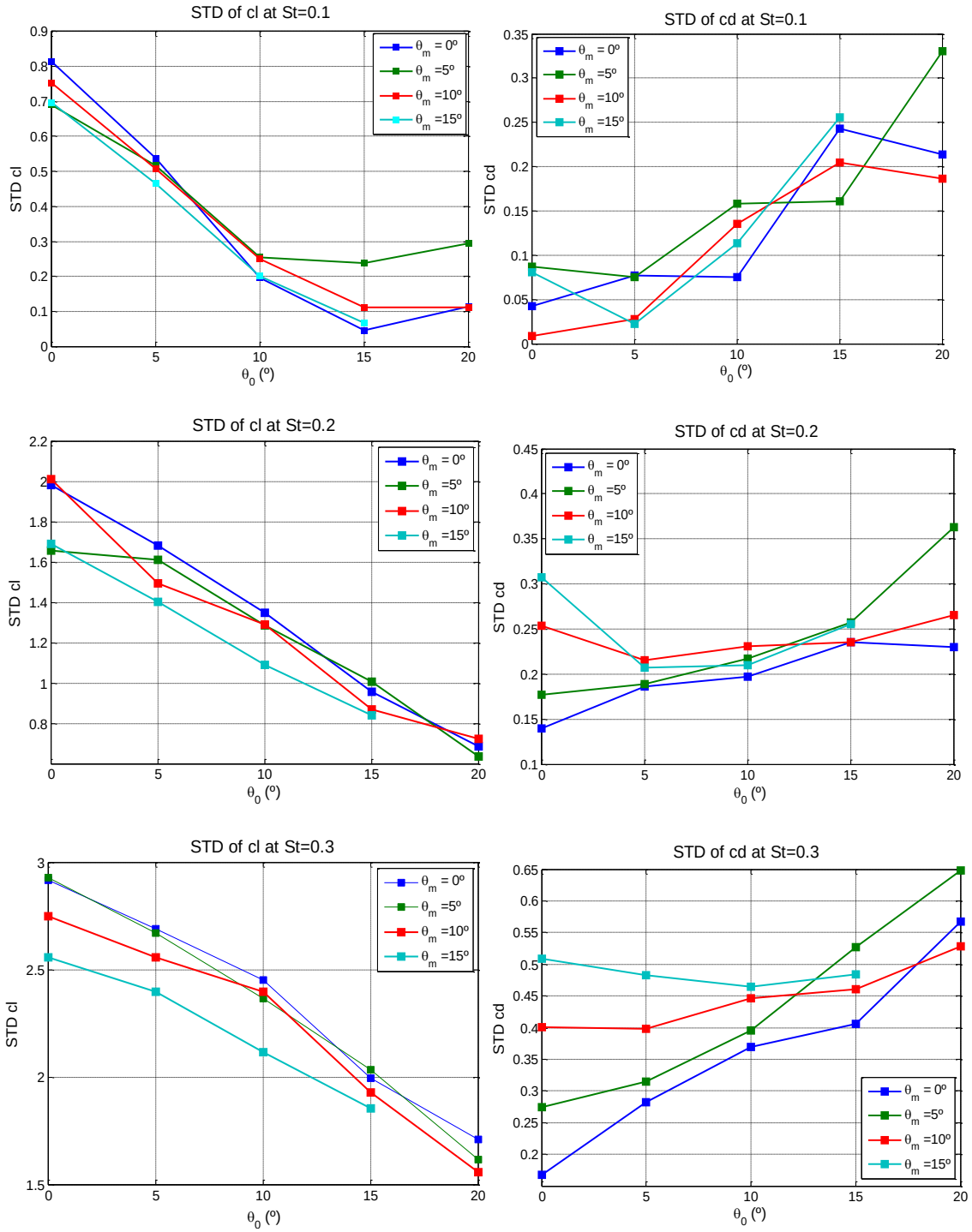

Figure 34. Standard deviations of the lift and drag coefficients for the different Strouhal numbers as a function of the pitch amplitude

The standard deviation in the lift coefficient decreases for increasing θ_0. The reason for this relies on the fact that as the pitching amplitude grows, the effective velocity that the airfoil experiences gets more aligned with the free-stream velocity (the effective angle of attack decreases), producing thus a lower fluctuation amplitude in the lift coefficient.

The opposite effect is found in the drag coefficient; the standard deviation grows with θ_0. However, it must be noticed that the drag coefficient standard deviation is approximately an order of maginitude smaller than the one of the lift coefficient.

In addition, another important feature is that the standard deviations are larger for greater Strouhal numbers due to the delayed LEV separation and consequent lift enhacement found in Baik et al. [23] and explained in section 6.2.3.

As a conclusion, in order to have a balance between the standard deviations in both force coefficients such that structural fatigue is avoid, a good approach would be choosing an intermediate pitching amplitude θ_0 and a low Strouhal number.

6.5. Mean lift and drag coefficients

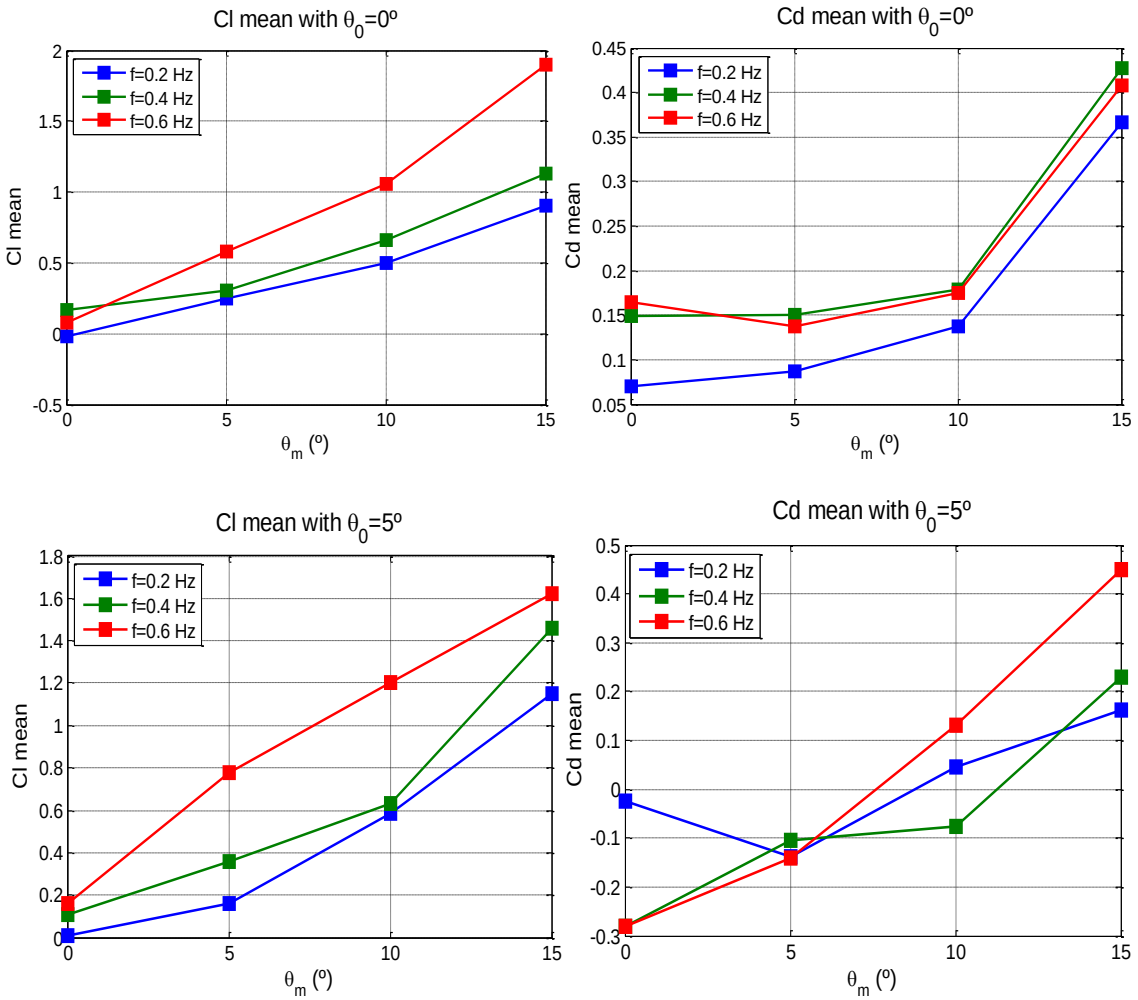

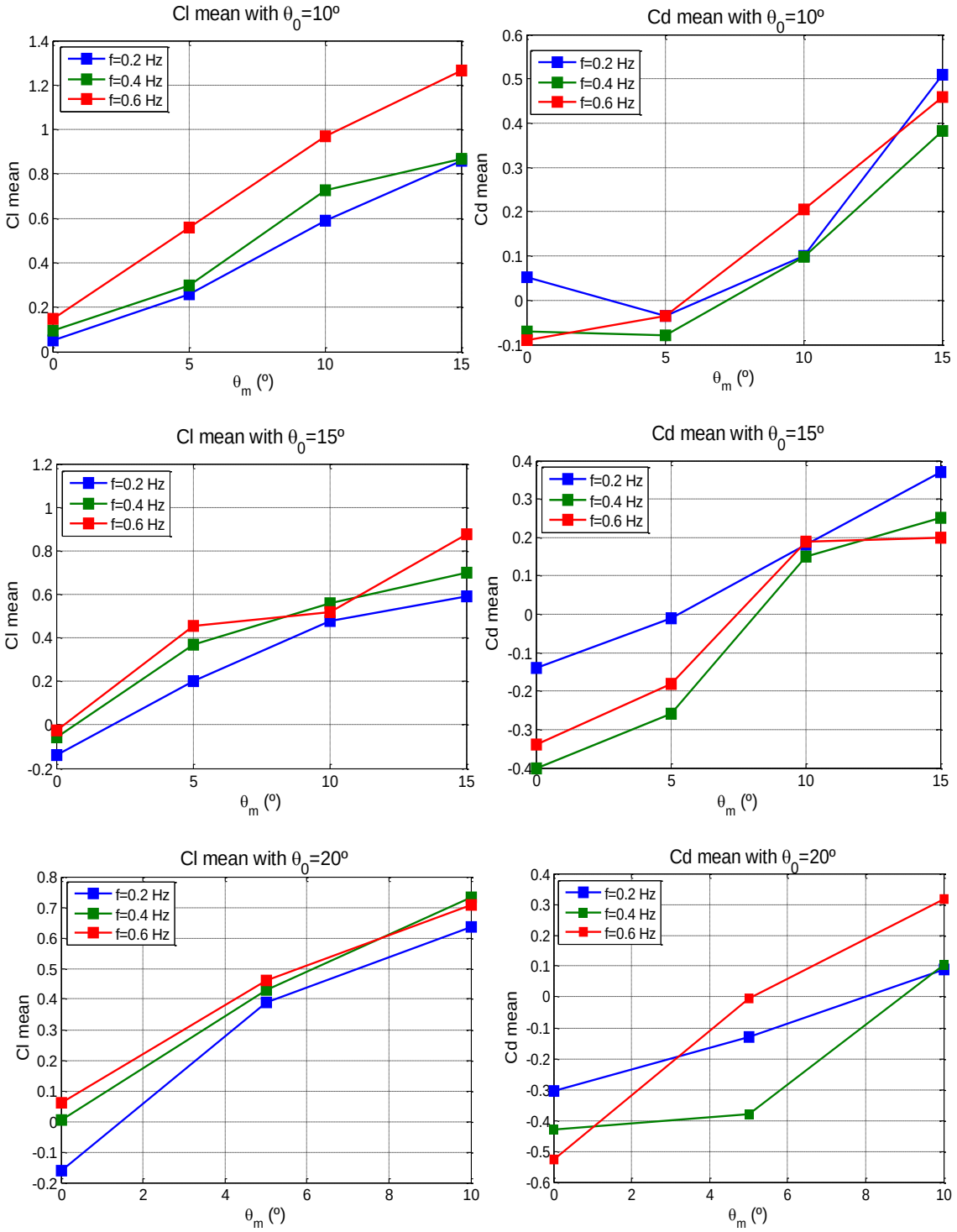

Figure 35. Mean force coefficients for the different Strouhal numbers as a function of the mean pitch angle.

Three main conclusions that can be gathered from the mean force results are as follows:

1. The mean lift and drag cofficients increase as the mean pitch angle increases, having the lift coefficient a more linear trend. In addition, the slope of the lift curves are greater than one of the steady lift polar.
2. The force coefficients are generally higher for the greatest Strouhal number, but this condition does not always hold.
3. If $\theta_0 > 5°$, the force coefficients generally decrease, being this effect stronger in the drag coefficient. In fact, the mean drag coefficient becomes negative (which means that thrust is generated) for $\theta_0 > 10°$ and low values of the mean pitch angle θ_m. This result is consistent with the observations made in section 6.3.1. However, if $\theta_0 < 5°$, there is a slight increase in the force coefficients.

According to this results, lift will be maximized if a low pitch amplitude and a high mean pitch angle is chosen, whereas thrust will be optimum for high amplitudes and low mean angles. They both coincide in having a large Strouhal number.

This results are obiously conditioned by the used procedure to remove the sensor bias, so the veracity of the conclusions is subjected to that.

7. CONCLUSIONS AND FUTURE WORK

After this work, some conclusions can be gathered in terms of what it is the best configuration for force generation. An "optimum" configuration can have different meanings depending in the target to be reached, i.e. maximum lift, minimum standard deviation…

Three optimum goals will be addressed:

1. For a maximum lift, the optimum would be a low pitch amplitude and a high mean pitch angle.
2. For a minimum drag (or thrust creation), the amplitude is required to be high and the mean angle low.

The greatest Strouhal number is the one giving the best force results in both cases.

3. In order to reach a relatively low standard deviation in both force coefficients in order to avoid structural fatigue, an intermediate pitch amplitude and a low Strouhal number is required.

Taking all of this into account, a design target must be chosen before selecting a flapping wing configuration.

In addition, as it was previously mentioned, the veracity of the reached conclusions in the work are subjected to the used procedure to remove the sensor bias. For this reason, the force measurements to calculate the mean force coefficients should be repeated using the right procedure in future works. In this way, the gathered conclusions will be verified or rejected.

8. TIME SCHEDULE AND BUDGET

8.1. Time schedule

This project as started in October 2016 and finished in September 2017 with a 6-months brake from February to July. The dedication was not uniform; it was lower from October to December and higher the rest of the time.

The timing has been divided in 4 parts:

8.1.1. Literature review

The first step was doing some research about the state-of-the-art of the flapping wing problem and summarizing the important points. This period took about 50 h of work counting with the reading and writing-up.

8.1.2. Problem and experimental set-up understanding

This phase concerned the comprehension of the followed procedure and the reasons why it was done in a particular manner. It took about 10 h summing up the tutor explanations and the personal work.

8.1.3. Experimental procedure

Doing all the tests took several days. The first tests were done in October and it was verified that they had physical sense. The rest of them were carried out between December and January. In addition, another set of shorter tests were made when the sensor heat transfer bias was noticed and before the problem with the sensor functioning was reported. The total time estimation is about 80 h.

8.1.4. Analysis of the results

This part was mainly done during January, August and September. An estimation of 50 h is given as several trials to do the calculations were needed due to the sensor problem.

8.1.5. Report write up

In order to write all the report and think about the physical meaning of the results, a total time of 200 h has been estimated.

8.1.6. Total time

Timeline	Amount of hours
Literature review	50
Problem understanding	10
Experimental procedure	80
Analysis of the results	50
Report write up	200
Total	390

Table 6. Time spent in the project.

8.2. Budget

To estimate the budget, the depreciation of the devices already existing at the university and the amortization of the new devices acquired for the development of this project will be accounted for.

The water tunnel was already in the university laboratory. Its price was 140000 € and it has a 6 years depreciation. This gives a total of 64. 5 € per day. This together with the water, electricity and other facilities it has been estimated as 200 € per day. It can be assumed that it was used for a total of 20 days, so it gives a total cost of 4000 €.

The bought equipment consists of a F/T sensor, the movement system parts, the wing model and other necessary components and tools.

The F/T sensor and the rest of the force measurement system have a 4 year amortization and it can be considered that they have been used for 10 months (from the start of the project). The price was 10000 €, giving a cost of 2080 €.

The movement system had a price of 6000 € with the same amortization. This gives a total of 1250 €.

The wing model had a cost of 100 €, this together with another components and tools needed for the development of the project gives an estimation of around 500 €.

Finally, the cost of the time spent by the student is quantified by setting an average salary of 12 € per hour. This gives a total of 4680 € for the 390 h used in this project.

The budget is summarized in the following table:

Item	Cost
Water tunnel use	4000 €
Force measurement system	2080 €
Movement system	1250 €
Wing & other components	500 €
Student time	4680 €
Total	12510 €

Table 7. Budget summary.

The estimation of the total cost of this project is of 12510 €.

9. ACKNOLEDGEMENTS

Firstly, I would like to express my gratefulness to Dr. Andrea Ianiro for giving me the opportunity of doing this project in the department. And specially to my tutor Marco Raiola for his help, understanding and support during the development of this thesis.

I would also like to thanks to all the professors that have helped me during my studies in University Carlos III of Madrid. Without their dedication, studying this bachelor would have been impossible.

And last, but not least, I am extremely grateful to my family and friends for encouraging me. Specially, I would like to mention to Paloma Maestro, Celia González, Iñigo Sainz and Ignacio de la Hera for their support during these 4 years.

10. REFERENCES

[1] Pines, D. J. & Bohorquez, F. "Challenges facing future micro-air vehicle development," *Journal of aircraft,* vol. 43, no. 2, pp. 290-305, 2006.

[2] Cummings, M.L., Jackson, P.Q., & Pitman, D."Development and Testing of a Quad Rotor Smartphome Control System for Novice Users"*International Journal of Micro Air Vehicles,* vol. 4, no.3, September 2012.

[3] Da Vinci, L. "Codex on the flight of birds", 1505.

[4] Knoller, R. "Air resistance laws".*Flug-und Motortechnik,* vol. 3, pp. 1-9, 1909.

[5] Betz, A. "A contribution to the explanation of the gliding flight". *Zeitschrift fuer angewandte Flugtechnik und Motorluftschiffahrt*, vol. 3, pp. 269-272, 1912.

[6] Theodorsen, T. "General theory of aerodynamic instability and the mechanism of flutter," *NACA Report 496,* 1935.

[7] Garrick, I. E. "Propulsion of a flapping and oscillating airfoil," *NACA Report* vol. 567*,* 1937.

[8] Von Kármán, T. and Sears, W.R. "Airfoil Theory for Non-Uniform Motion," *Journal of the Aeronautical Sciences,* vol. 5, no. 10, pp. 379-390, August 1938.

[9] Chang, C. C. "Potential flow and forces for incompressible viscous flow". *In Proc. R. Soc. Lond.* A, vol. 437, pp. 517-525, 1992.

[10] Martín-Alcántara, A., Fernández-Feria, R. & Sanmiguel-Rojas, E. "Vortex flow structures and interactions for the optimum thrust efficiency of a heaving airfoil at different mean angles of attack". *Phys. Fluids*, 2015.

[11] Moriche, M., Flores, O. García Villalba, M., "On the aerodynamic forces on heaving and pitching at low Reynolds number," *Journal of Fluid mechanics*, July 2017.

[12] Lewin, G. C. & Haj-Hariri, H. "Modelling thrust generation of a two-dimensional heaving airfoil in a viscous flow". *J. Fluid Mech.*, vol. 492, pp. 339-362, 2003.

[13] Berg van den, C. & Ellington, C. P. "The Three Dimensional Leading Edge Vortex of a 'Hovering' Model Hawkmoth". *Philosophical Transactions of Royal Society of London*, vol. 352, pp. 329-340, 1997.

[14] W.J. McCroskey, L.W. Carr. & K.W. McAlister. "Dynamic Stall Experiments on Oscillating Airfoils". *AAIA Journal*, 1976.

[15] Carr, L. W. "Progress in analysis and prediction of dynamic stall". *Journal of Aricraft*, 1988.

[16] Leishman, J. G. "Principles of Helicopters Aerodynamics". pp. 429-431., 2000.

[17] Dickinson, M. H. & Gotz, K. G. "Unsteady aerodynamic performance on model wings at low Reynolds numbers," *Journal of Experimental Biology,* vol. 174, pp. 45-64, 1993.

[18] Gharib, M., Rambod, E. & Shariff, K., "A Universal time scale for vortex ring formation," *Journal of Fluid Mechanics,* vol. 360, pp. 121-140, 1998.

[19] Krueger, P.S. & Gharib, M., "The significance of vortex ring formation to the impulse and thrust of a starting jet" *Physics of fluids,* vol. 15, pp. 1271, 2003.

[20] Daibiri, J. O, "Optimal vortex formation as a unifying principle in biological propulsion," *Annual Review of Fluid Mechanics*, vol. 41, pp. 17-33, 2009.

[21] Anderson, J. M., Streitllein, K., Barret, D. S. & Triantafyllou, M. S.,"Oscillating foils of high propulsive efficiency," *Journal of Fluid Mechanics,* vol. 360, pp. 41-72, 1998.

[22] Read, D. A., Hover, F.S. & Triantafyllou, M.S. "Forces on oscillating foils for propulsion and maneuvering," *Journal of Fluid and structures,* vol. 17, pp. 163-183, 2003.

[23] Baik, Y. S, Bernala, L.P., Granlunda, K. & Ol, M. V. "Unsteady force generation and vortex dynamics of pitching and plunging aerofoils," Journal of Fluid Mechanics, vol. 709, pp. 37-68, 2012.

[24] Ley 31/1995, de 8 de noviembre de Prevención de Riesgos Laborales (BOE nº 269 de 10 de noviembre).

[25] Real Decreto 39/1997, de 17 de enero, por el que se aprueba el Reglamento de los Servicios de Prevención (BOE nº 27 de 31 de enero).

[26] Buckingham, E. "On physically similar systems; Illusstrations of the use of dimensional equations," Physical review, vol. 4, no. 4, pp. 345, 1914.

[27] A. I. A. "Nano-17 IP68 sensor webpage," [Online]. Available: http://www.ati-ia.com/products/ft/ft_models.aspx?id=Nano17+IP65%2fIP68.

[28] Moral Maroto, P. "Design and water tunnel testing of a flapping wing", 2015.

[29] Sunada, S., Yasuda, T., Yasuda, K., Kawachi, K. "Comparison of Wing Characteristics at an Ultralow Reynolds Number"vol. 39, no. 2, 2002.

[30] Leishman, J. G. "Principles of Helicopters Aerodynamics". pp. 533-535., 2000.

11. ANNEX

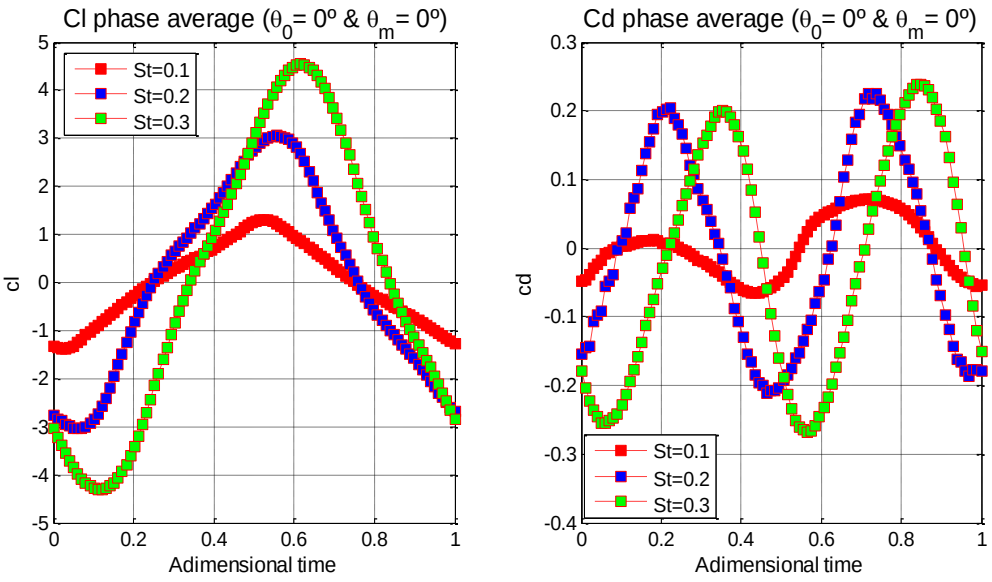

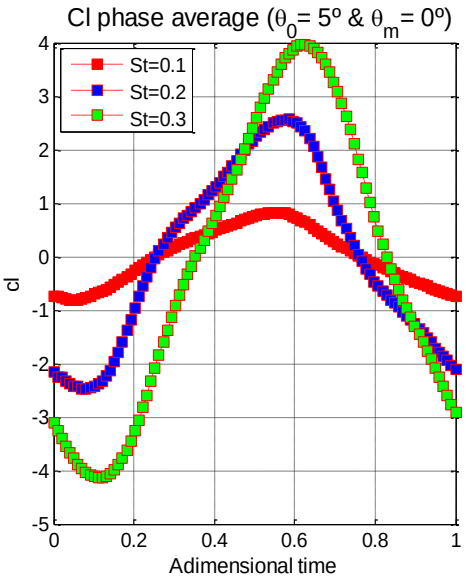
Cl phase average (θ_0= 5º & θ_m= 0º)
St=0.1
St=0.2
St=0.3
cl
Adimensional time

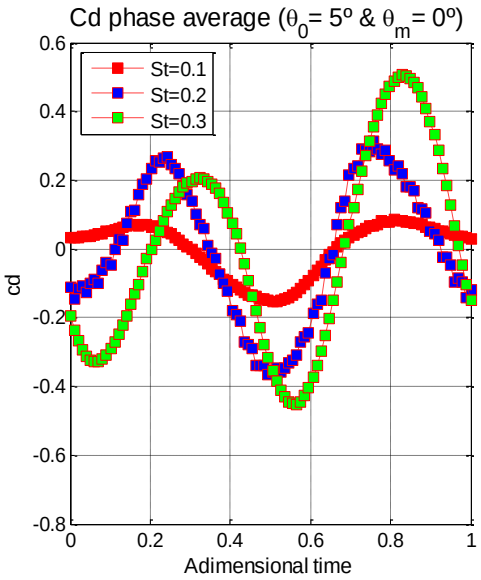
Cd phase average (θ_0= 5º & θ_m= 0º)
St=0.1
St=0.2
St=0.3
cd
Adimensional time

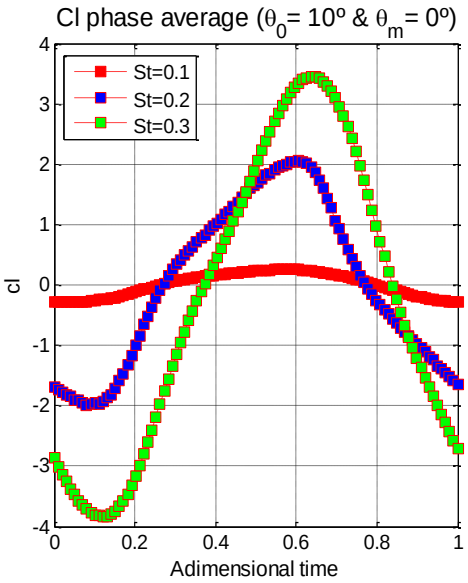
Cl phase average (θ_0= 10º & θ_m= 0º)
St=0.1
St=0.2
St=0.3
cl
Adimensional time

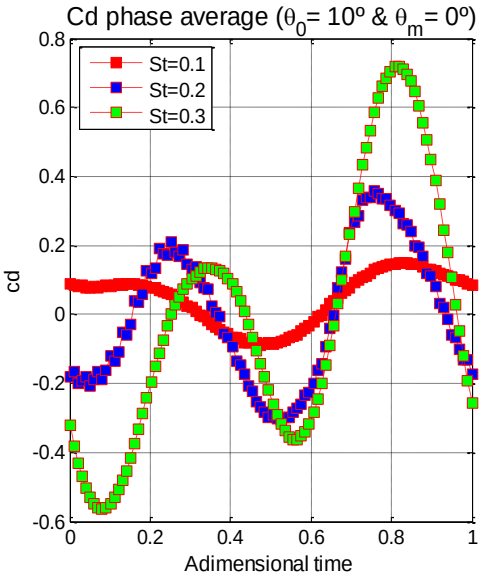
Cd phase average (θ_0= 10º & θ_m= 0º)
St=0.1
St=0.2
St=0.3
cd
Adimensional time

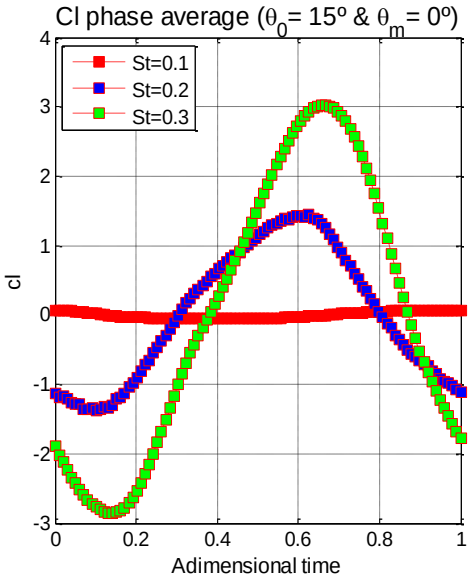
Cl phase average (θ_0= 15º & θ_m= 0º)
St=0.1
St=0.2
St=0.3
cl
Adimensional time

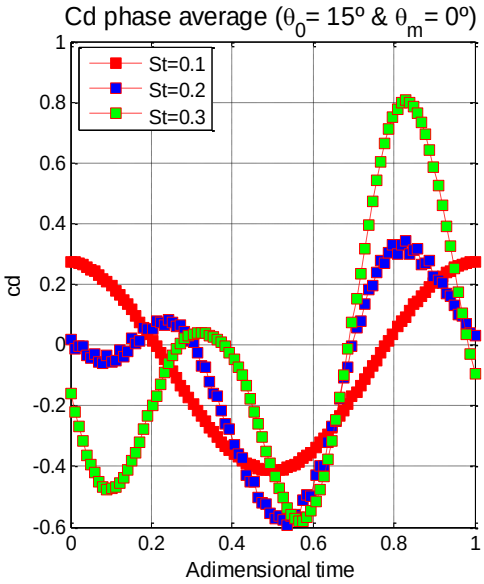
Cd phase average (θ_0= 15º & θ_m= 0º)
St=0.1
St=0.2
St=0.3
cd
Adimensional time

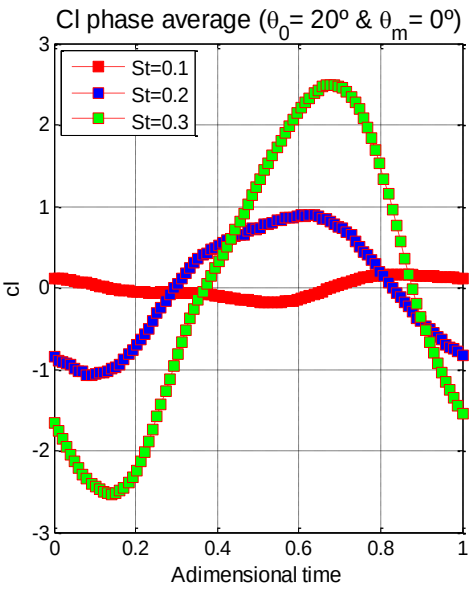
Cl phase average (θ_0= 20º & θ_m= 0º)
St=0.1
St=0.2
St=0.3
cl
Adimensional time

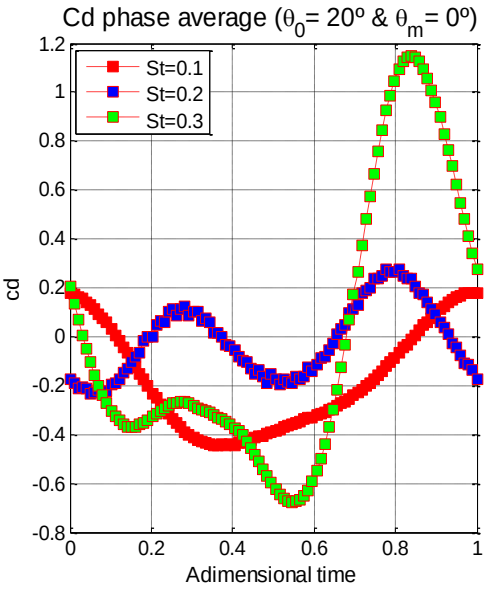
Cd phase average (θ_0= 20º & θ_m= 0º)
St=0.1
St=0.2
St=0.3
cd
Adimensional time

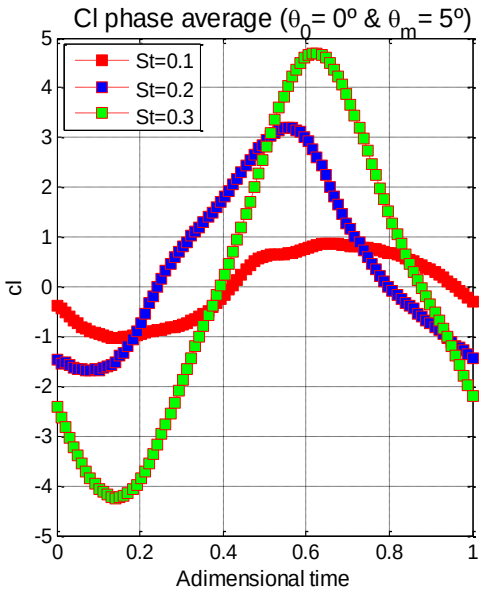
Cl phase average (θ_0= 0º & θ_m= 5º)
St=0.1
St=0.2
St=0.3
cl
Adimensional time

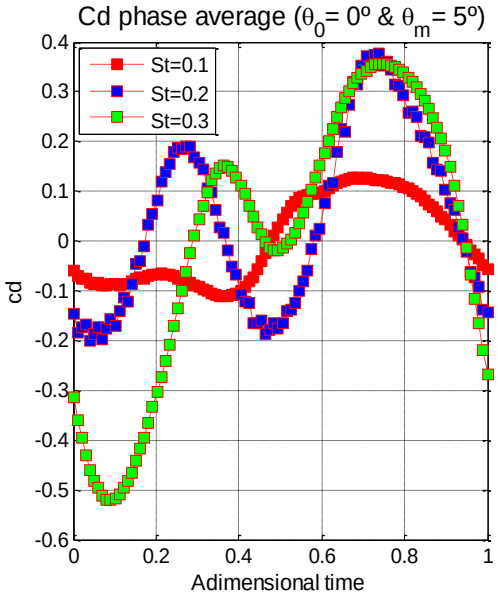
Cd phase average (θ_0= 0º & θ_m= 5º)
St=0.1
St=0.2
St=0.3
cd
Adimensional time

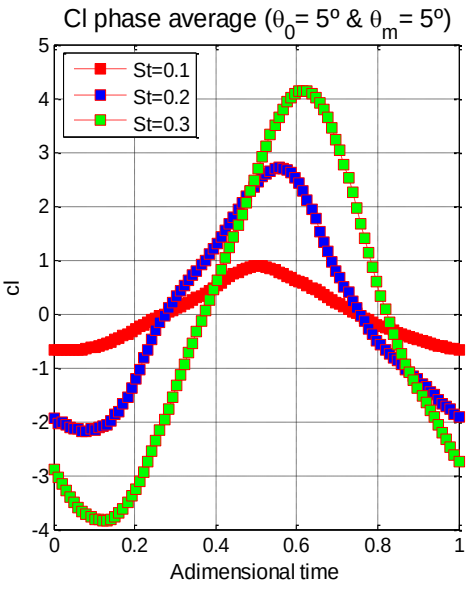
Cl phase average (θ_0= 5º & θ_m= 5º)
St=0.1
St=0.2
St=0.3
cl
Adimensional time

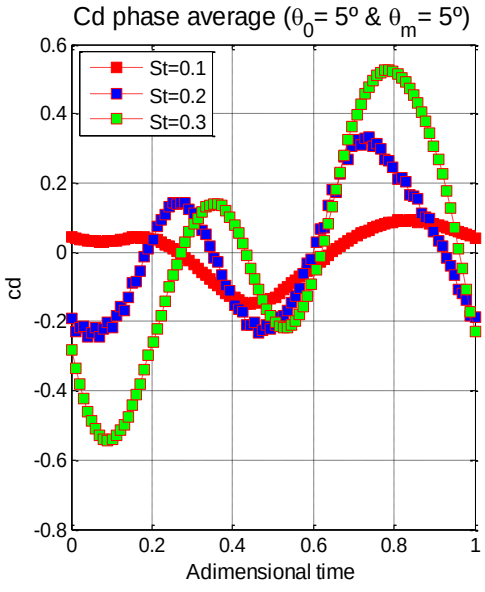
Cd phase average (θ_0= 5º & θ_m= 5º)
St=0.1
St=0.2
St=0.3
cd
Adimensional time

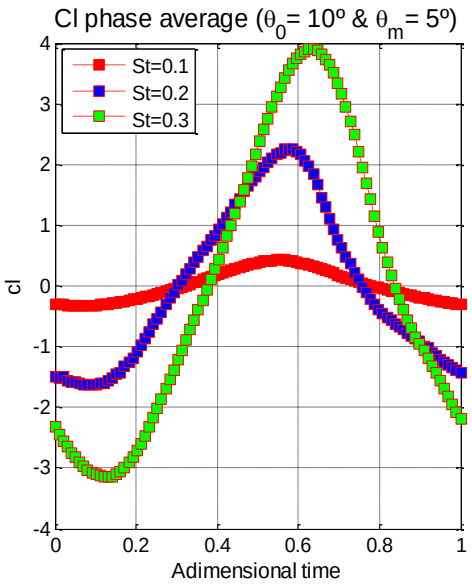
Cl phase average (θ_0= 10º & θ_m= 5º)
St=0.1
St=0.2
St=0.3
cl
Adimensional time

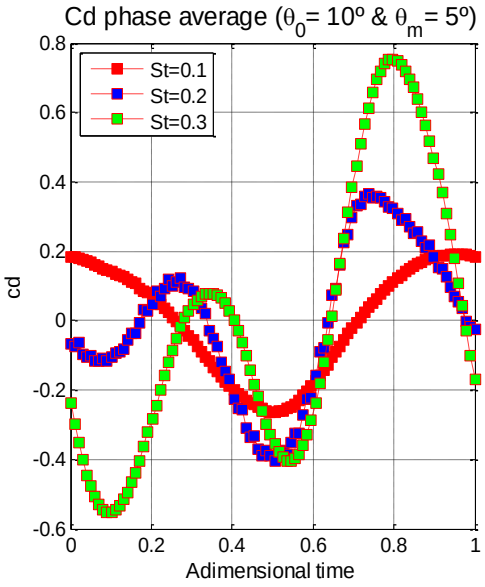
Cd phase average (θ_0= 10º & θ_m= 5º)
St=0.1
St=0.2
St=0.3
cd
Adimensional time

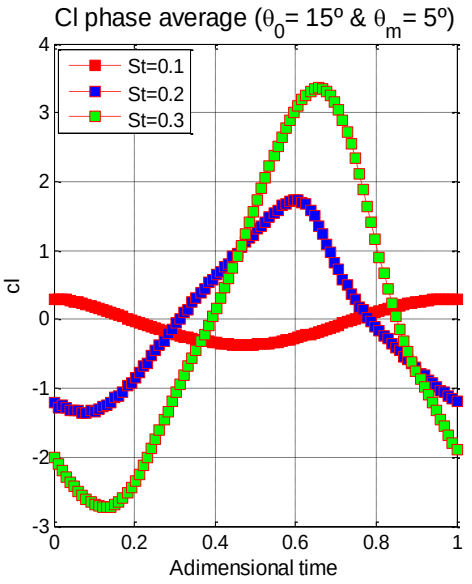
Cl phase average (θ_0= 15º & θ_m= 5º)
St=0.1
St=0.2
St=0.3
cl
Adimensional time

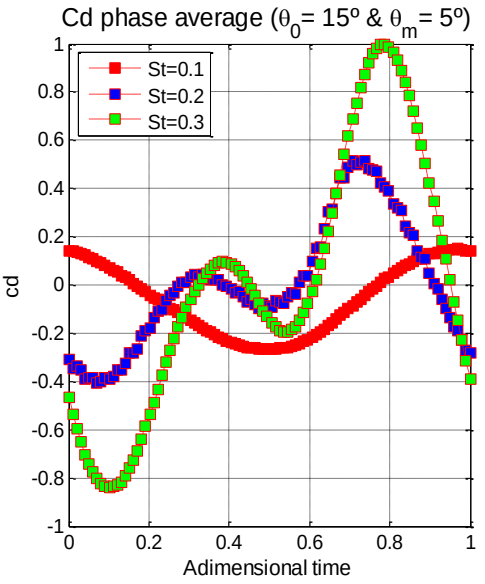
Cd phase average (θ_0= 15º & θ_m= 5º)
St=0.1
St=0.2
St=0.3
cd
Adimensional time

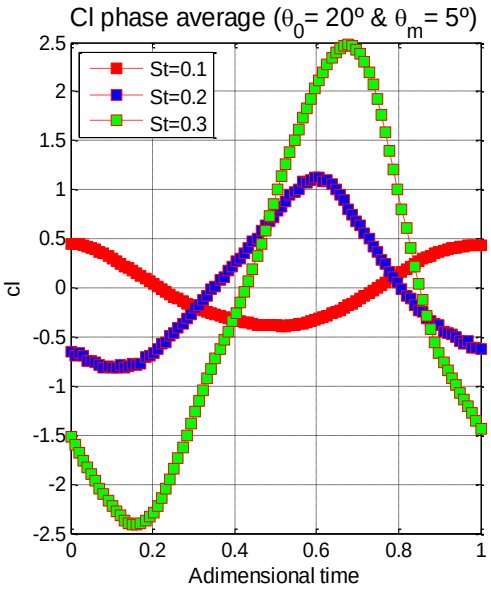
Cl phase average (θ_0= 20º & θ_m= 5º)
St=0.1
St=0.2
St=0.3
cl
Adimensional time

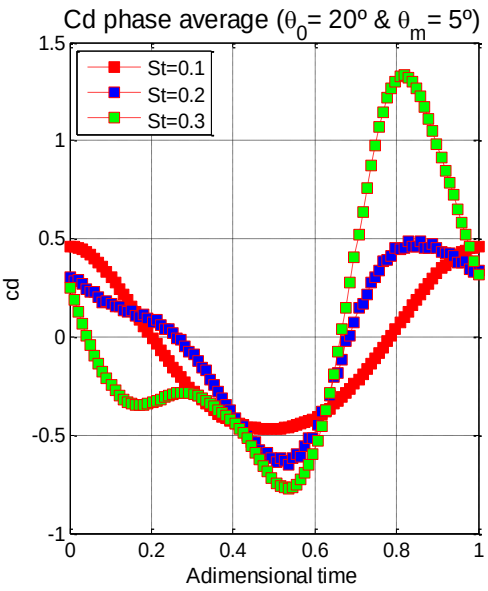
Cd phase average (θ_0= 20º & θ_m= 5º)
St=0.1
St=0.2
St=0.3
cd
Adimensional time

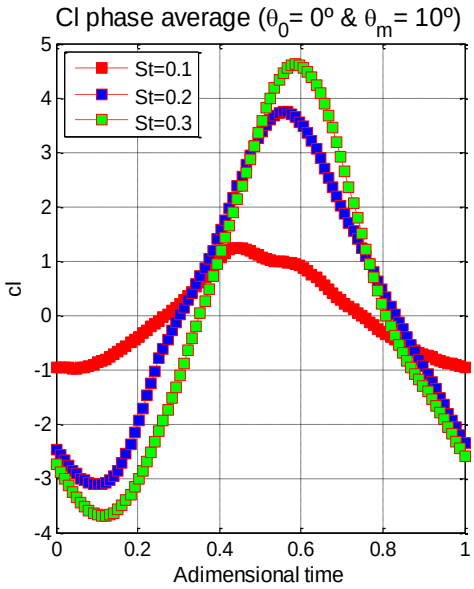
Cl phase average (θ_0= 0º & θ_m= 10º)
St=0.1
St=0.2
St=0.3
cl
Adimensional time

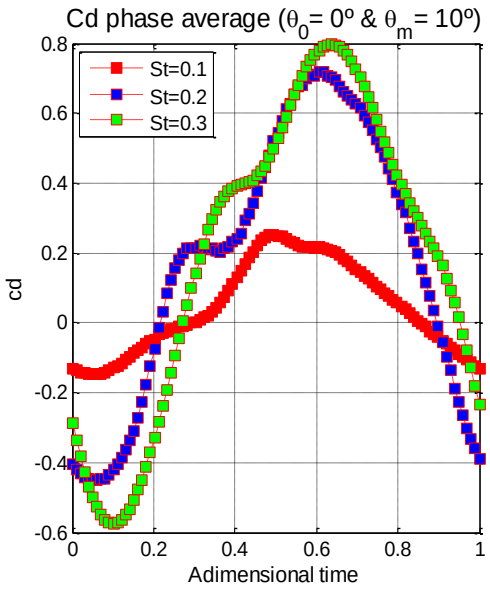
Cd phase average (θ_0= 0º & θ_m= 10º)
St=0.1
St=0.2
St=0.3
cd
Adimensional time

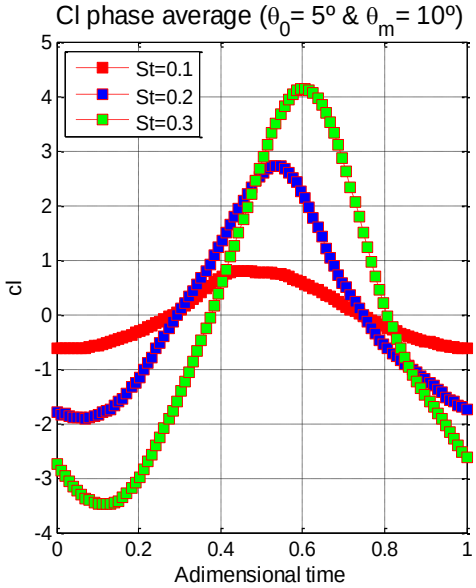
Cl phase average (θ_0= 5º & θ_m= 10º)
St=0.1
St=0.2
St=0.3
cl
Adimensional time

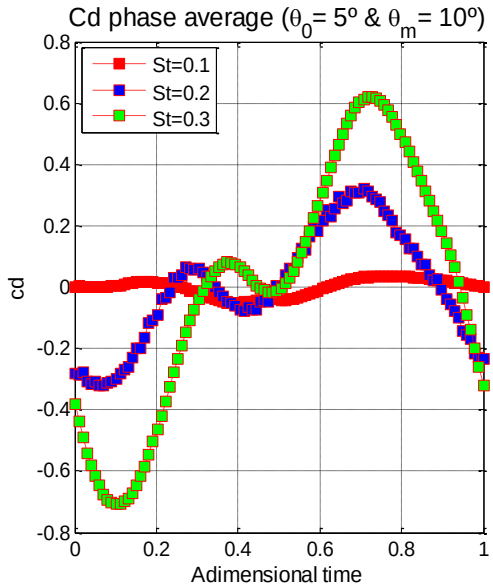
Cd phase average (θ_0= 5º & θ_m= 10º)
St=0.1
St=0.2
St=0.3
cd
Adimensional time

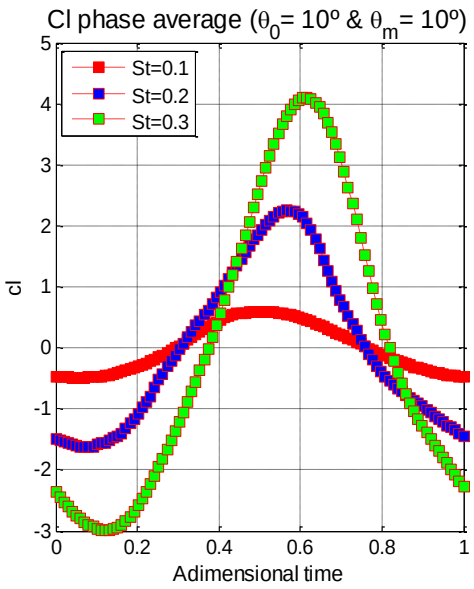
Cl phase average (θ_0= 10º & θ_m= 10º)
St=0.1
St=0.2
St=0.3
cl
Adimensional time

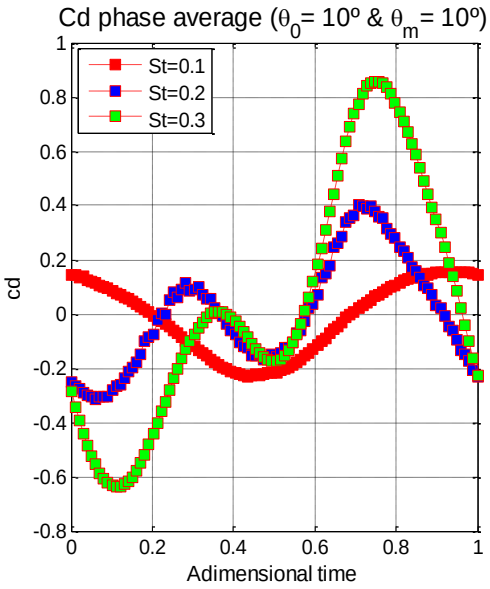
Cd phase average (θ_0= 10º & θ_m= 10º)
St=0.1
St=0.2
St=0.3
cd
Adimensional time

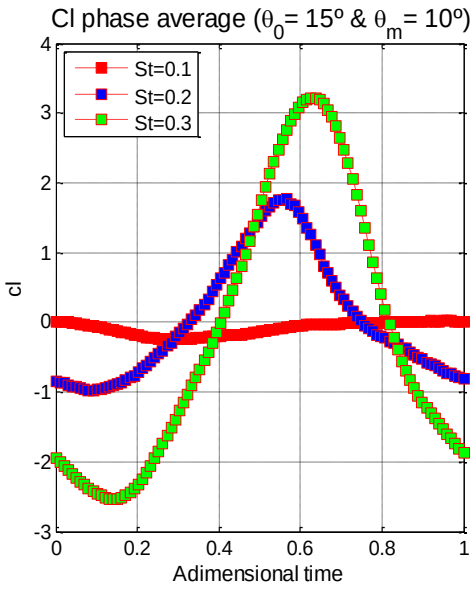
Cl phase average (θ_0= 15º & θ_m= 10º)
St=0.1
St=0.2
St=0.3
cl
Adimensional time

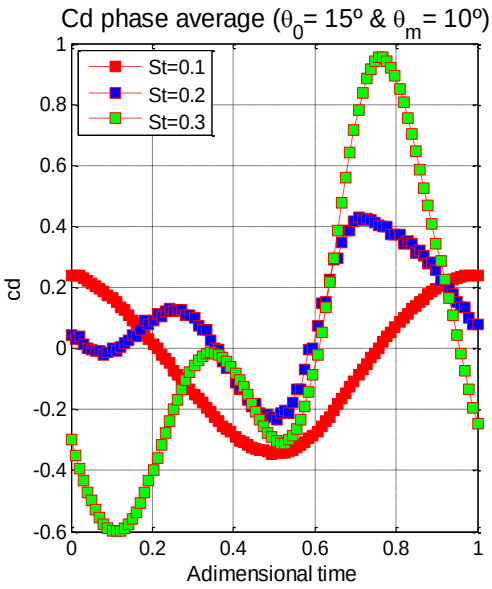
Cd phase average (θ_0= 15º & θ_m= 10º)
St=0.1
St=0.2
St=0.3
cd
Adimensional time

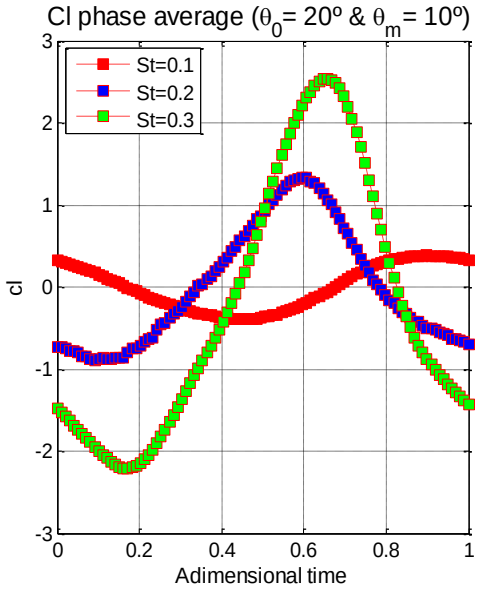
Cl phase average (θ_0= 20º & θ_m= 10º)
St=0.1
St=0.2
St=0.3
cl
Adimensional time

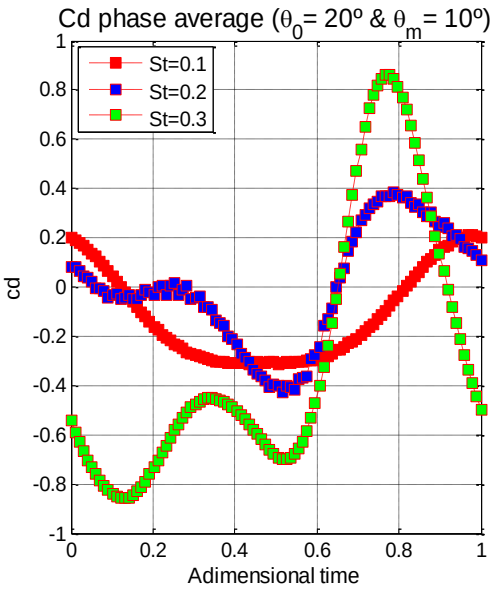
Cd phase average (θ_0= 20º & θ_m= 10º)
St=0.1
St=0.2
St=0.3
cd
Adimensional time

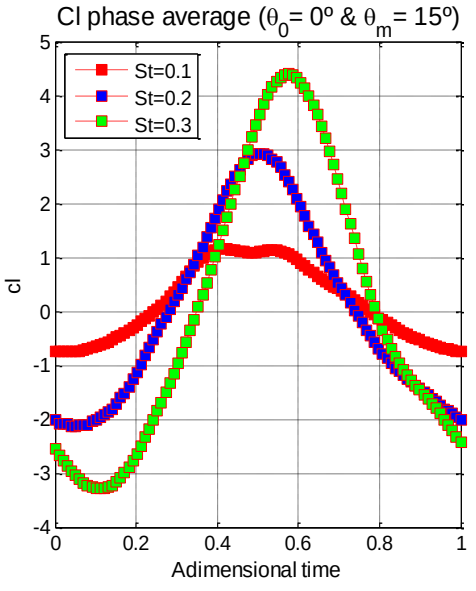
Cl phase average (θ_0= 0º & θ_m= 15º)
St=0.1
St=0.2
St=0.3
cl
Adimensional time

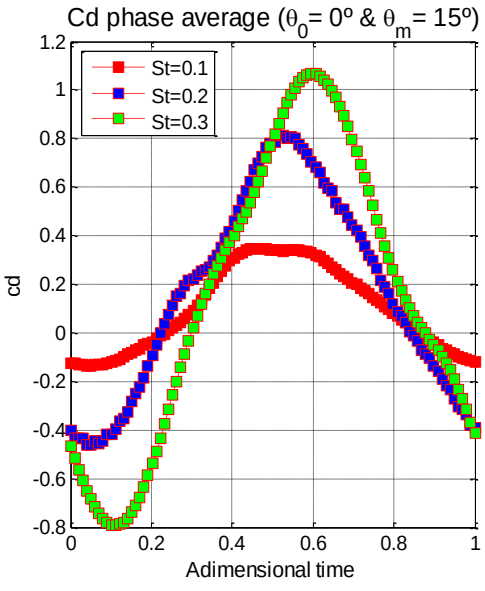
Cd phase average (θ_0= 0º & θ_m= 15º)
St=0.1
St=0.2
St=0.3
cd
Adimensional time

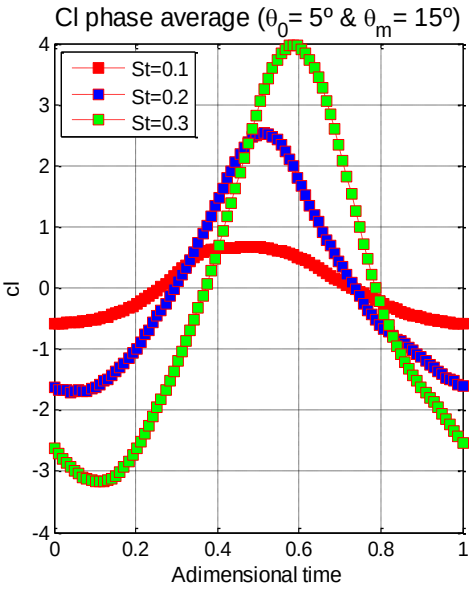
Cl phase average (θ_0= 5º & θ_m= 15º)
St=0.1
St=0.2
St=0.3
cl
Adimensional time

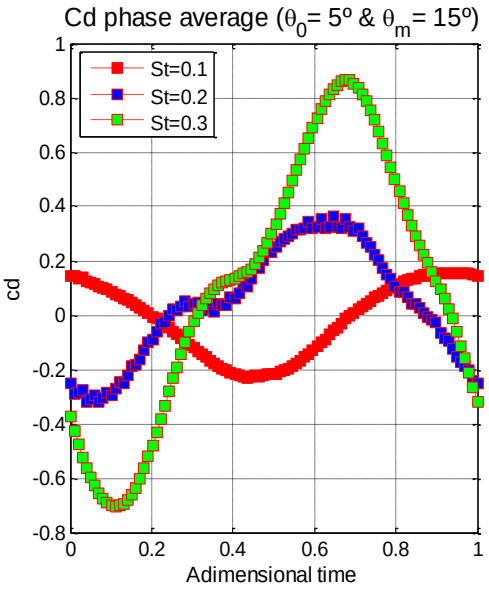
Cd phase average (θ_0= 5º & θ_m= 15º)
St=0.1
St=0.2
St=0.3
cd
Adimensional time

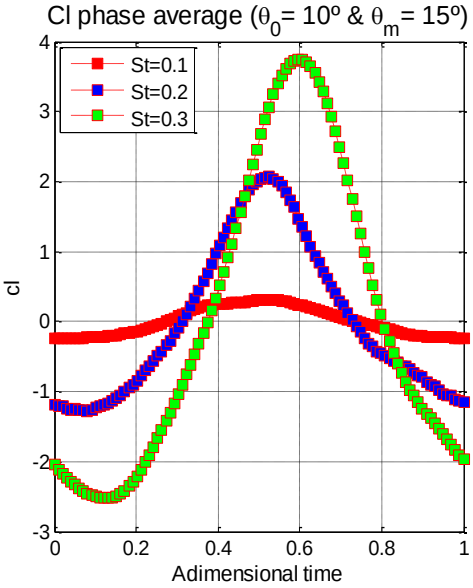
Cl phase average (θ_0= 10º & θ_m= 15º)
St=0.1
St=0.2
St=0.3
cl
Adimensional time

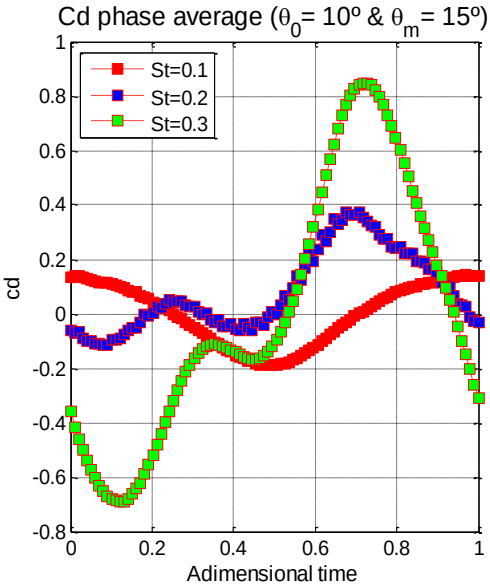
Cd phase average (θ_0= 10º & θ_m= 15º)
St=0.1
St=0.2
St=0.3
cd
Adimensional time

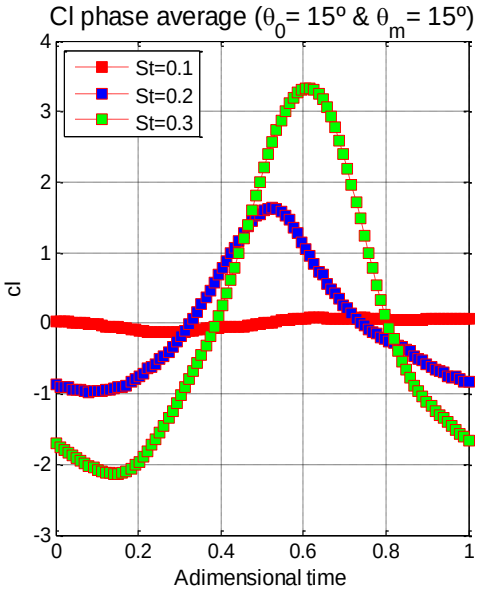
Cl phase average (θ_0= 15º & θ_m= 15º)
St=0.1
St=0.2
St=0.3
cl
Adimensional time

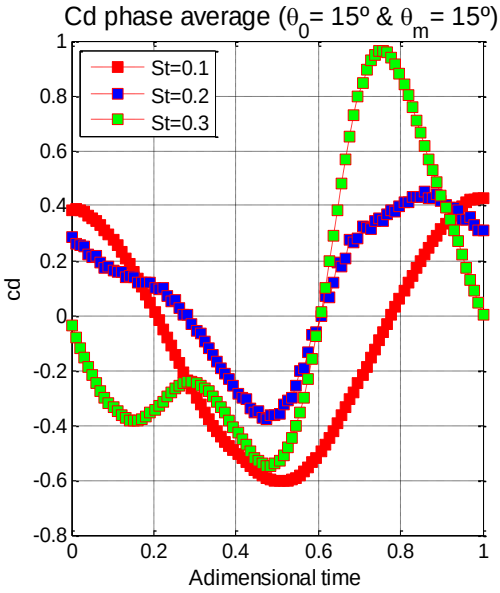
Cd phase average (θ_0= 15º & θ_m= 15º)
St=0.1
St=0.2
St=0.3
cd
Adimensional time